INVESTIGATION INTO POLYMER BONDED EXPLOSIVE DYNAMICS UNDER GAS GUN IMPACT LOADING

by

Jonathan D. Drake

A Thesis

Submitted to the Faculty of Purdue University

In Partial Fulfillment of the Requirements for the degree of

Master of Science in Aeronautics and Astronautics

School of Aeronautical and Astronautical Engineering

West Lafayette, Indiana

May 2020

THE PURDUE UNIVERSITY GRADUATE SCHOOL
STATEMENT OF COMMITTEE APPROVAL

Dr. Weinong W. Chen, Chair
School of Aeronautics and Astronautics

Dr. Steven F. Son
School of Mechanical Engineering

Dr. Jeffrey F. Rhoads
School of Mechanical Engineering

Approved by:
Dr. Gregory A. Blaisdell

In Dedication to my wife and parents

ACKNOWLEDGMENTS

The author would like to thank C. S. Blum-Sorensen, N. Kedir, A. Leenig, K. Stirrup, S. C. Paulson, C. D. Kirk, Z. Guo, and J. O. Mares of Purdue University for their experimental help as well as T. Sun, N. D. Parab, A. Deriy, P. Shevchenko, and K. Fezzaa of Argonne National Laboratory for their assistance with the x-ray imaging as well, as Dr. Mauro Sardela of the University of Illinois at Urbana-Champaign for help with Laue Back Reflection X-ray Diffraction. The author would also like to recognize Dr. Weinong Chen, Dr. Steven Son and Dr. Jeffrey Rhoads for their support and guidance throughout this project. This work was supported by the Office of Naval Research under the award number N00014-16-1-2557 to Purdue University.

TABLE OF CONTENTS

LIST OF TABLES

LIST OF FIGURES

ABSTRACT

The initiation of high explosives (HEs) under shock loading lacks a comprehensive understanding: particularly at the particle scale. One common explanation is hot spot theory, which suggests that energy in the material resulting from the impact event is localized in a small area causing an increase in temperature that can lead to ignition. This study focuses on the response of HMX particles (a common HE) within a polymer matrix (Sylgard-184®), a simplified example of a polymer bonded explosive (PBX). A light gas gun was used to load the samples at impact velocities ranging from 370 to 520 m/s. The impact events were visualized using X-ray phase contrast imaging (PCI) allowing real-time observation of the impact event. The experiments used three subsets of PBX samples: multiple particle (production grade and single crystal), drilled hole, and milled slot. Evidence of damage and deformation occurred in all of the sample types. While the necessary impact velocity for consistent hot spot formation leading to reactions was not reached, the damage (particularly cracking) that occurred provides a useful indication of where hot spots may occur when higher velocities are reached. With the multiple particle samples, evidence of cracking and debonding occurred throughout. One sample showed significant volume expansion due to possible reaction. The samples containing drilled holes demonstrated the expected pore collapse behavior at these velocities, as well as damage downstream from the holes under various two-hole arrangements. Milled slot samples were tested to simulate existing cracks in the HMX. These samples showed increased damage at the site of the milled slot, as well as unique cracking behavior in one of the samples.

1. INTRODUCTION

The response of energetic materials under impact loading, particularly when ignition occurs, is of great interest to military and civilian organizations. As munitions increase in energy potential, the need for those munitions to be insensitive (that is to have a low sensitivity) is vital [1-3]. While creating energetic materials with varying threshold energies for ignition is of some use, it is widely observed that energetic materials can ignite at energies lower than the desired threshold [2]. On the particle level, it is not completely understood what mechanism or mechanisms lead to ignition, providing a need for investigation. While several mechanisms have been proposed, the most widely accepted is the hot spot theory.

Hot spot theory has been the dominating proposed theory for explosive reaction that occurs at insufficient energy levels for decades [4]. This theory predicts that the necessary energy for ignition under impact loading comes from energy consolidation caused by damage and deformation [1]. Essentially, some mechanism (or combination of mechanisms) occur in the material that causes thermal energy to concentrate in a microscopic region of critical volume, allowing that particular region to reach ignition temperatures. The term came about after it became clear that energetic materials could be ignited at energy levels insufficient to raise the bulk material to the necessary temperature to expect ignition [5]. Upon the formation of the hot spot, it can either fail (not reach the critical energy) or react to form an ignition site in the energetic material [6]. These ignition sites do not necessarily mean that the bulk material will detonate, they can deflagrate (burn) or they can contribute to a growing shockwave that could lead to a larger reaction [7, 8]. The end result of a hot spot is a factor of various chemical and physical properties through a selection of debated hot spot mechanisms [6].

Considerable research has been conducted on the mechanisms involved in hot spot formation and growth over the last several decades. These proposed mechanisms essentially detail the conversion of mechanical or electrical energy into thermal energy [7]. In 1948, Bowden and Yoffe looked into three expected mechanisms for hot formation in both liquid and solid energetic materials: frictions, collapse of gas spaces, and viscous heating, finding all to be viable [4]. Later in 1982, Coffey and Armstrong at the Naval Surface Weapons Center explored what the specific mechanisms involved in hot spot formation may look like. Their work largely focused on the effects of dislocation movements in the formation of hot spots. They found that

looking purely at the macroscopic level was not sufficient because the phenomena became more localized as the strain rates increased. At the microscopic level, it can be noted that dislocation pile-ups, often at grain boundaries, can cause localized increases in temperature [5].

This research was continued and expanded upon by many, including Field et al. in 1992 who used several experimental methods to make their own observations about the hot spot mechanisms [7]. This group looked at ten separate proposed mechanisms for the formation of hot spots including the dislocation pileup theory proposed by Armstrong and Coffey. Following from this work, they sought to see if the energy created by dislocation pile-ups was sufficient to cause ignition and found that to be unlikely. They theorized that the observations of Coffey and Armstrong could have come from adiabatic shear [7]. After going through the various mechanisms, they found that the most likely mechanisms were the adiabatic shear just mentioned alongside heating of trapped gases in collapsing cavities. Field et al. also recognized that the dominating mechanism may be different based on the material type and structure and that mechanisms may act additively to create critical hot spots [7].

In 2002, M.R. Baer at Sandia National Laboratories continued this work by taking into consideration that almost all energetics in use are heterogeneous: often a combination of an energetic crystal and a polymer binder [9]. As a shock wave contacts a subject, various materials act differently driven by their properties, thus the formation and growth of a potential hot spot in a heterogeneous material would occur differently (and in a more complex manner) than a homogeneous material. This particular research focused on a modeling approach with statistical analysis and mesoscale modeling of random close packed configurations of polyhedral crystals [9]. While the research found that some tools necessary to accurately model these events did not yet exist, they did find that some of the above mechanisms were in play [9].

The discussion to this point has focused on the general hot spot theory. This thesis will focus on the hot spot formation specifically in a composite HMX energetic material. First off, HMX is the common name cyclotetramethylene tetranitramine, an explosive crystal. Furthermore, these crystals are most often found in a PBX, or polymer-bonded explosive. PBXs are widely used in weapons systems and are formed with 80-95% of a high explosive particle dispersed in a polymer matrix [10]. These energetic materials are not immune to the lower energy ignition caused by hot spots upon shock deformation and their sensitivity is dependent on several factors primarily driven by the filler molecule, which in this case, are the HMX particles

[11]. Among the most vital mechanisms are particle-particle or particle-matrix interactions [1, 3, 9, 12-16], the collapse of voids [4, 11, 16-25], and frictional heating [26-29].

The first subset of hot spot mechanisms surrounds the interactions between multiple particles in a PBX, as well as the interactions between the particles and the polymer matrix. This is very important as PBXs consist of many HE particles contained in a matrix. In 2004, Czerski and Proud took a deep look into the morphology of HMX particles and their relationship to the shock sensitivity [12]. They found that while the bulk morphology (particle density and size) had little effect on the shock sensitivity, the individual particle morphology did [12]. Furthermore, in 2004, Antoine and Bouma determined that the shock sensitivity was further dependent on the synthesis method and the surface quality [13]. They determined that a smooth surface could lessen shock sensitivity, changing the initiation pressure from 3.3 GPa to 3.9 GPa. Next, Bellitto and Melnik expanded on this work by looking specifically at the surface defects in HEs and determined that the surface defects made a "statistically significant" impact on the shock sensitivity [3]. Baer and Trott approached these concepts while looking at heterogeneous PBXs, a more complex analysis [9]. Using mesoscale modeling, they put together random HMX particles in a polymer binder and modeled them under varying impact conditions [9]. They started with inert HMX particles at an impact speed of 1000 m/s to study the thermo-mechanical behaviors (here the conditions surely would produce the energy necessary for reaction). They found that the stress fields within the material fluctuated significantly because of the varying surface interactions due to the heterogeneous nature of the subject [9]. Once the reactivity of the particles was added back into the model, the results went as expected. Where the localization occurred in the inert model, reaction occurs and causes even larger pressure fields in the sample [9].

Another mechanism tied to hot spot formation is the collapse of voids. There is a direct correlation between the sensitivity of energetic materials and the relative amount of internal voids [1]. While the collapse of a void can contribute to the formation of a hot spot in multiple ways, the most prominent is the formation of a hydrodynamic jet that sends a hot liquid to the downstream end of the void [24]. In 2018, Wood et al. comprehensively characterized the nature of void collapses in HEs using computer modeling (while this is Hexanitrostilbene, HNS, and not HMX, the behavior is expected to be similar, although at differing velocities and pore sizes [22]). They determined that the pore collapse would likely occur in progressive modes ranging from

viscoplastic at lower shock pressures to hydrodynamics at higher shock pressures [22]. The viscoplastic collapse occurs relatively uniformly around the pore, while the hydrodynamic collapse folds inwards producing a liquid region that "jets" into the rest of the material [22]. This "jetting" only forms during the collapse of a void at high pressure but can contribute heavily to hot spot formation [22]. Figure 1.1 shows a representation of three collapse modes as well as a graph of what pressure and pore size these collapses happened in their models (recall this is in HNS not HMX).

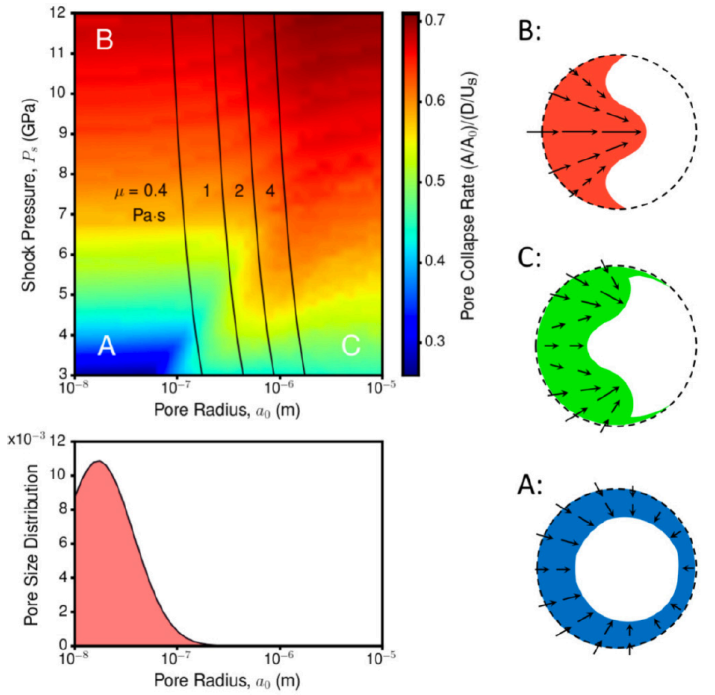

Figure 1.1. Color map of collapse modes in HNS using mesoscale modeling. The blue region (A) is viscoplastic collapse and the red region (B) is hydrodynamic with jetting [22].

There are two additional critical properties of these voids to note: the size and distribution. In general, it is observed that particles with very small voids are difficult to ignite; therefore the critical temperature (temperature required for a hot spot to grow) increases drastically as the void diameter decreases [6]. Hua et al. analyzed the effect of defect size on the shock heat using discrete element analysis, simplifying the defect to be a sphere [20]. In their investigation they found that as the shock pressure increased, the highest temperature localizations shifted from the defects with a radius of about 35 μm to those with a radius of about 30 μm [20]. This shows that

the small defect sizes will begin to have bigger effects on the hot spot formation as the shock pressure increases; however, they still found that the large void sizes have the largest effect on the localized temperature increases [20]. Several years later, Zhau et al. continued this line of research using modeling methods. The data showed, as expected that when there were no voids, there was little to no temperature increase; yet as the defect size increased, so did the maximum temperature. By these simulations, it appears that with a void size of about 4 to 5 nm (radius), there is a significant increase in the thermal energy due to the plastic work as the shock wave collapses the void (see figure 1.2) [1]. The data also showed that after the shock wave passed; the temperature began to decrease again at a rapid rate after only 5 ps if the hot spot did not grow. Combining these results, Zhau predicted that with a void size diameter of less than 2 nm, the hot spot will likely fail to grow, those in the range of 2-5 nm may fail or succeed, and those above 5 nm have a high probability of growing [1]. Additionally, with the increased temperatures found with the larger void size, Zhau predicted that more violent chemical reactions would result from larger voids [1].

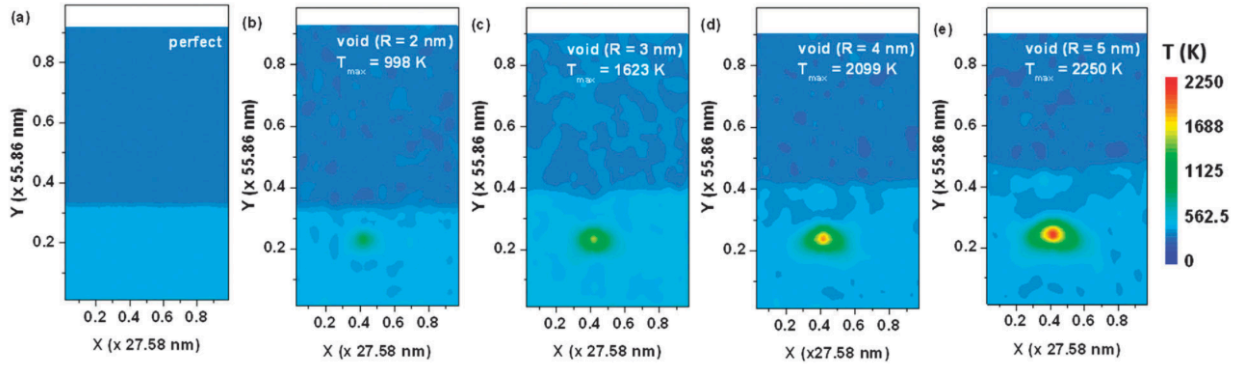

Figure 1.2. The spatial distributions of temperature at the time of hot spot formation for crystals with various sized voids under an impact velocity of 1 km s^{-1} [1].

The other major factor is the distribution of the voids. Kapahi and Udaykumar took a comprehensive look into how the relative position of the voids could effect hot spot formation. To start, they ran simulations on two distributions composed of two voids [21]. First, they looked at two voids in line with the incoming shock wave as seen on the left in figure 1.3. This shows that the second void actually collapses with a lower resulting temperature than the first void, thus not contributing to the formation of a hot spot [21]. While this may seem counterintuitive, they note that it occurs because the first void shields the second, and the local increase in temperature

surrounding the first void softens the impact on the second void [21]. This means that a void directly behind an additional void will not increase the sensitivity of the material because it can only form a lower temperature hot spot than the first void. It should be noted that these voids are within a diameter apart, increasing shielding, and it is theorized that as the voids are moved further apart, the shielding effect would decrease [21]. Next, they looked at two voids staggered in line with the shock wave as seen on the right in figure 1.3. Here they found the opposite effect, the collapse of the second void led to a higher temperature hot spot [21]. They reason that this occurs because, with no shielding from the first void, the second void feels the entire effect of the shock wave with the addition of a secondary wave created by the collapse of the first void [21]. From here, Kapahi and Udaykumar looked at a more complicated model of a HMX crystal with several voids scattered in the sample. The results of the simulations showed that the phenomena found with the in-line and staggered voids held to be true, meaning that some shielding occurred with in line voids, and increased temperatures could be seen with staggered ones [21]. In the end, they found that more voids led to a greater conversion of kinetic energy to thermal energy (as expected), however as the process was very localized, the maximum temperature did not increase past that expected of the two voids in tandem [21].

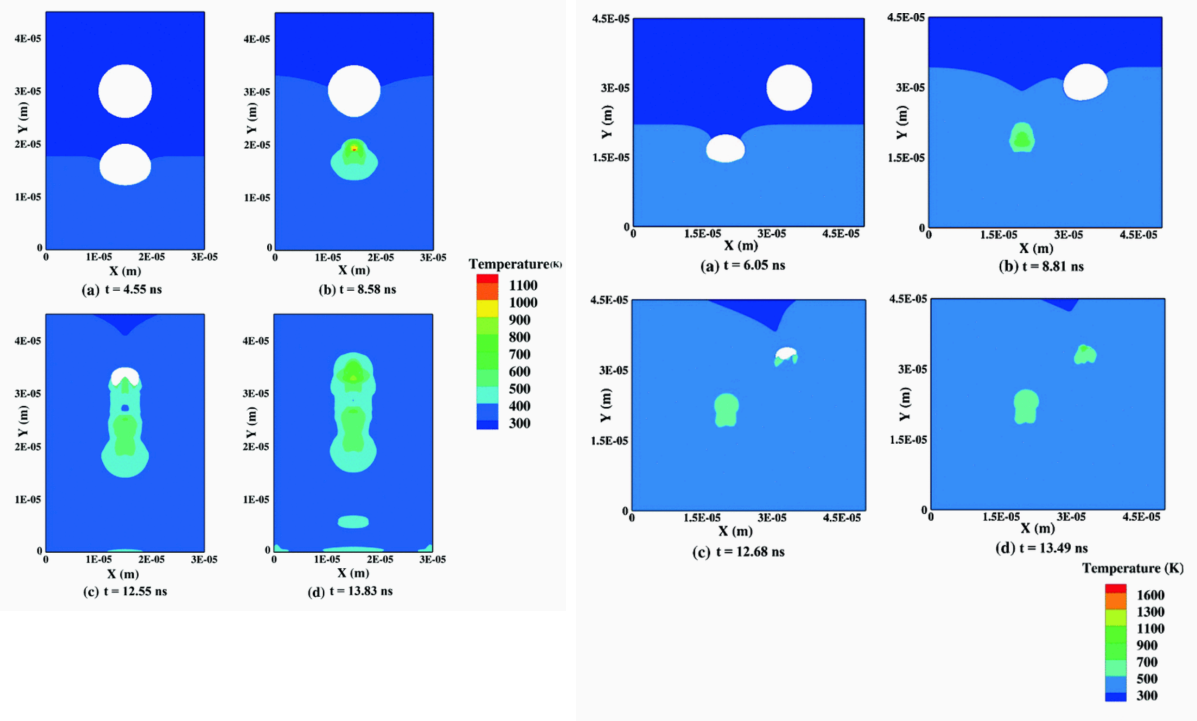

Figure 1.3. Inline voids (left) and offset voids (right) impacted from the bottom of the image [21].

Another proposed factor to the formation and growth of hot spots centers around frictional heating and energy dissipation: specifically near cracks. In 2006, Dienes et al. looked into the ignition of explosives due to crack mechanics. This paper used a statistical approach to model the response of cracks under dynamic loading, testing the hypothesis that "the intense heating by frictional sliding between the faces of a closed crack during unstable growth can form a hot spot, causing localized melting, ignition, and fast burn of the reactive material adjacent to the crack [26]." After running several different experiments through the model, it showed that the hot spot formation and growth near cracks due to shear forces proved to be a viable mechanic, as well as a great explanation for ignition in stress regimes too low for the spherical void collapse to be a viable mechanism [26].

In 2017, Tanasoui and Koslowski expanded on the work of Dienes et al. noting that the energy dissipation caused by fracture is a vital mechanism to the formation and growth of hot spots under impact loading [27]. Their computational study focused on determining the effect of the critical energy release rate on the damage and energy dissipation, as well as the effect of cracks on the damage and dissipation. In the study, a simulation was run on the same model (containing four HMX particles in a polymer matrix) first with no initial defects and second with initial defects in the form of cracks seen in figure 1.4. Tanasoui and Koslowski's model agreed with Dienes et al., showing that with the addition of the initial cracks, there was a significant increase in the potential for damage in the sample under impact loading [27].

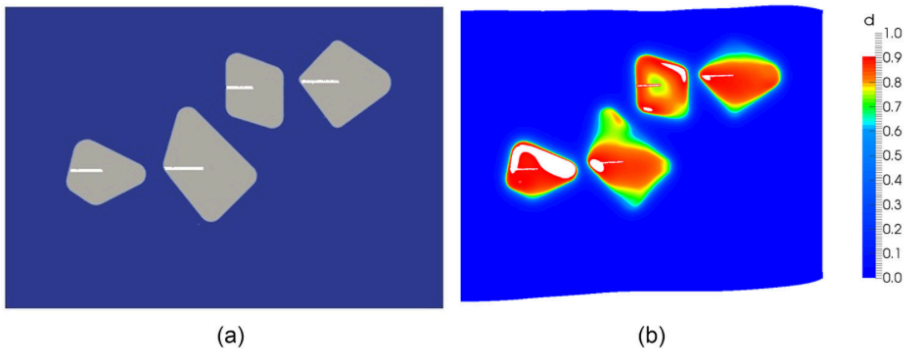

Figure 1.4. Predicted damage at a critical energy release rate of 5 J/m^2 with initial cracks [27].

Finally, in 2018 Duarte et al. continued by looking at initial cracks in HMX particles in a Sylgard matrix under impact loading at 100 m/s and 400 m/s: the latter in the regime of the experiments in this work [28]. This research looked at the impact of three factors on the temperature increases in the model: crack length, crack density, and impact velocity. It was found that while initial crack length and crack density has limited effect, impact velocity is essential as none of the 100 m/s impacts produced likely hot spots, while the 400 m/s impacts did (see figures 1.5 and 1.6) [28]. Notably, it was found in conjunction with a previous paper that the highest temperature increases occurred where the cracks intersected the particle-polymer interface, such as the samples presented in this paper [28, 29].

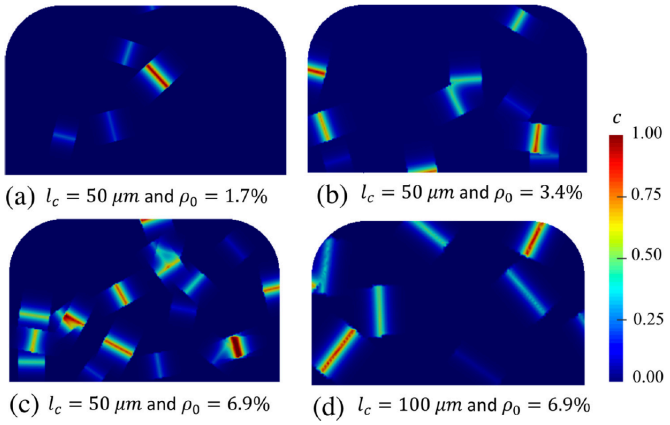

Figure 1.5. Initial crack distributions present in the particles [28].

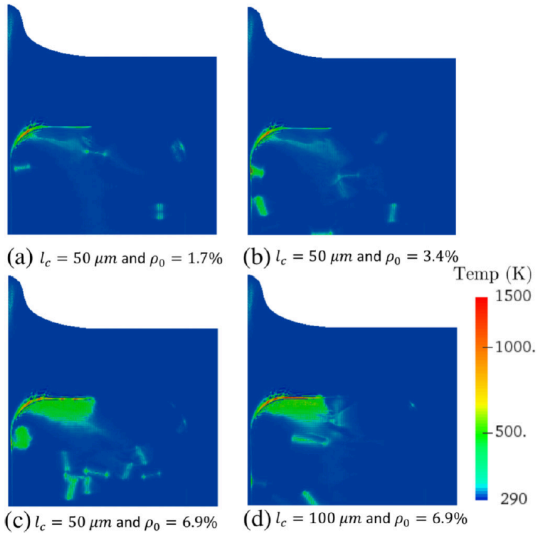

Figure 1.6. Temperature field at t = 0.28 μs impacted at 400 m/s [28].

One additional detail to note is the crystal orientation of the HMX particles (particularly as most of the experiments discussed here contain single crystals). Several of the studies mentioned above specify the crystal orientation of the impacted face, as this can change the impact response [23, 28, 30]. One such study by Grilli and Koslowski in 2018 titled "The effect of crystal orientation on shock loading of single crystal energetic materials" looked at the orientation effects in samples similar to those discussed here [30]. One of their tests looked at a single crystal containing a cylindrical hole in three different crystal orientations: (011), (-1-11), and (010). When impacted, they found that these crystals all deformed differently and produced different temperature fields [30]. In future work, particularly with single crystal samples, the crystal orientation will be an important factor.

Since the inception of research in this area, a few major difficulties have always been present. Some of these issues, such as deciding on what assumptions to make during modeling, are not discussed in detail here, but perhaps the largest obstacle with experimental methods is the inability to directly observe the phenomena. In 1996, Tarver et al. noted this issue and was forced to qualify their research by disclosing methods to estimate certain conditions. "Since hot spot temperatures and dimensions cannot be measured experimentally, these estimated temperatures, sizes, and times required for exothermic chemical reaction provide a means to evaluate proposed physical mechanisms of hot spot formation in accident scenarios involving impact (friction and shear) and shock compression of solid explosives [6]." More recently, Zhou et al. commented that "currently, direct experimental observation of void collapse in shocked real explosives is extremely difficult due to the high strain rates, the resulting high temperature and pressure, and the extremely small relevant spatial-temporal scales over which void collapse occurs, and also because the phenomena of interest occur in the bulk of an optically impenetrable material [1]." New methods, however, have made it possible to look at the sample directly when it is impacted.

One example of such methods is the use of X-ray phase contrast imaging (PCI), which allows the direct observation of the inside of a sample during impact [10, 23, 31-45]. X-ray PCI works by passing X-rays through a material and measuring the phase shift in the X-rays on the other side of the material (rather than the attenuation in conventional X-ray imaging) [34]. This allows the researcher to see the particle damage, possible reactions, and deformation in real time. This technique has been used to image deformation in many materials with several impact

methods including similar gas gun work on HMX particles. One such work by N. Kerschen at Purdue University used the same experimental setup as described in this thesis on single HMX particles not containing engineered defects, both single crystal and production grade samples [10]. First, a selection of samples was impacted at about 200 m/s and noticeable cracking occurred (more prominent in the production grade samples as expected). As the impact velocity was increased, the cracking became progressively more severe until the peak velocity of 445 m/s was reached. At this velocity, debonding also occurred in addition to the cracking behavior [10]. Additionally, at this velocity volume expansion could be seen originating from the cracks. The author predicted that this might have occurred as a result of expanding gases from a reaction in the particles, however this also could be the result of crack expansion. Most importantly, this work showcases the ability of X-ray PCI to view a high-speed impact event in an opaque material. This capability continues to advance as further experience allows for more precise timing and clearer images. This work continues where the Kerschen paper leaves off and begins to examine the more complex situation of multiple particles in the matrix as well as the added damage present from initial engineered defects.

2. MATERIALS AND METHODS

Table 2.1. Experimental details.

Sample	Sample Description	Impact Velocity (m/s)	Tomography	Back Plate Material	Preparation Method
Figure 3.2	Multi-particle production HMX	420	No	Aluminum	Petri dish
Figure 3.3	Multi-particle production HMX	429	No	Aluminum	Petri dish
Figure 3.4	Dual-crystal HMX	443	No	Aluminum	Rectangular prism
Figure 3.5	Dual-crystal HMX	488	No	Aluminum	Rectangular prism
Figure 3.6	Dual-crystal HMX	432	No	Aluminum	Rectangular prism
Figure 3.7	HMX Crystal – 500 μm hole	463	Yes	Aluminum	Pipet
Figure 3.8	HMX Crystal – 500 μm hole	453	Yes	Aluminum	Pipet
Figure 3.9	HMX Crystal – Two 100 μm holes	370	Yes	Steel	Pipet
Figure 3.10	HMX Crystal – Two 100 μm holes	520	Yes	Steel	Pipet
Figure 3.11	Bare HMX Crystal – Two 200 μm holes	472	No	Steel	Pipet
Figure 3.13	HMX Crystal – 100 μm slot	458	Yes	Steel	Pipet
Figure 3.14	HMX Crystal – 80 μm slot	439	No	Steel	Pipet
Figure 3.15	HMX Crystal – 100 μm slot	490	Yes	Steel	Pipet
Figure 3.16	HMX Crystal – 100 μm slot	427	Yes	Steel	Pipet

2.1 Sample Preparation

The work described here covers various sample types described in the table above. Below, the various aspects of the sample preparation are discussed. It should be noted that not every sample went through all of the steps of the process; this is noted in the table above. First a particle was formed and cut to the specification for the particular experiment. Following this, a few samples underwent Laue Back Reflection X-ray Diffraction. Finally, the sample was (in most cases) encased into a polymer matrix using one of three methods described in detail below.

2.1.1 Sample Composition

The HMX crystals for of all the experiments (other than the two samples containing production grade particles which were purchased) were synthesized at Purdue University. These low defect HMX crystals were purified and crystallized at Purdue University resulting in single crystals, which were then cut down to a simplified geometry. In the case of the two single crystal samples, the samples were cut to create a generally flat interface between the crystals, as well as

a normal plane to the impact direction. The crystals are all β-HMX, the most stable of the four HMX polymorphs and also the one with the highest density [13]. The matrix material for all the samples that contained a polymer consisted of Sylgard-184®. Sylgard-184® has a number average molecular weight of 6,190 g/mol and a weight average molecular weight of 27,700 g/mol giving a polydispersity index (ratio of weight average to number average) of 4.47 [46]. To make the Sylgard-184® the elastomer and hardener were mixed in a 10:1 ratio and then degassed in a vacuum chamber. For some samples, 0.25 wt% Fe_2O_3 was added to provide better contrast under the PCI imaging [10]. The choice of curing time and temperature were chosen to maximize the elastic modulus (this increases with curing temperature) while remaining under transition temperature of the PE sheaths discussed in section 2.1.6 [47].

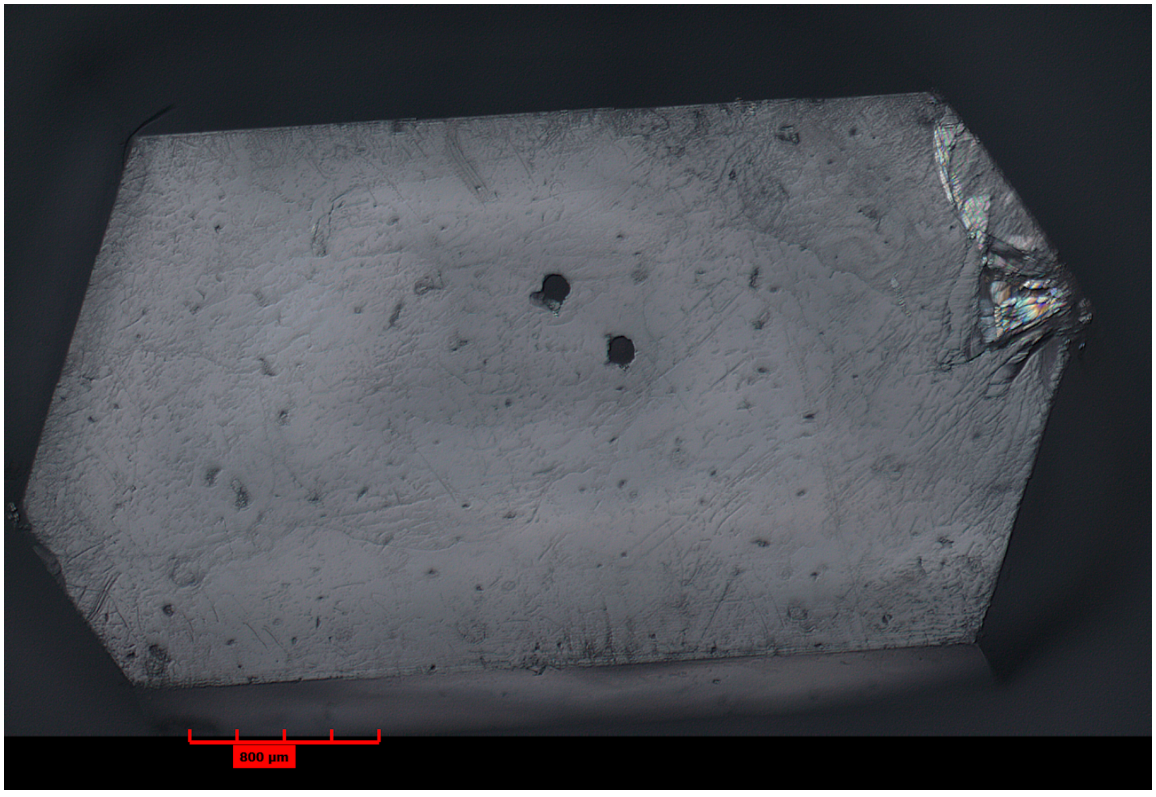

Figure 2.1. Image taken from optical microscope of the HMX crystal shown in figure 3.10.

2.1.2 Laue Back Reflection XRD

As discussed previously, the crystal orientation is important in order to analyze possible hot spot formation mechanisms [23, 28, 30, 48]. This presents a large challenge due to the size of the crystals and the complex nature of the HMX crystal structure. First, the size of the crystal prevents traditional indexing forms. This narrows the possible characterization techniques to a single XRD method called Laue Back Reflection. This method utilizes a detector sharing a plane with the X-ray source (normal to the emitted X-rays). The X-rays interact with the sample and the detector analyzes only the backwards-reflected X-rays. This forms a 2D diffraction map where darker spots appear where a high concentration of X-rays return. The spots on the map can be analyzed, once the crystal parameters are defined, to show which crystal face is normal to the X-ray beam. The second challenge is due to the HMX crystal structure: monoclinic tetragonal. The beta angle can make it difficult to decipher which plane is being scanned since several planes appear very close together. This method only became available for use in this work recently, thus only a single sample discussed here underwent this process. Furthermore, more work is needed to refine the data to provide complete confidence in declaring the orientation.

For this work, a partnership was formed with the Materials Research Lab at the University of Illinois at Urbana-Champaign to use a Laue System with a Multiwire® 2D detector. This system used a non-monochromatic Tungsten source for the X-ray beam and allowed for several beam sizes determined by the choice of collimator. All of the scans were taken at a distance of 150 mm from the X-ray source to the face of the bare HMX crystal (before engineered defects were added). The scans were analyzed using a Northstar® software that provided the original diffraction 2D pattern as well as a stereographic projection that can provide not only the orientation of the scanned face, but also the rotation angles to reach any desired plane (see figures below). In order to inform the system, the parameters found in table 2.2 were used (determined by indexing a smaller HMX particle synthesized with the same method at Purdue [49]). More analysis of these patterns can be seen in section 3.3.

Table 2.2. Lattice Parameters for β-HMX

Parameter	Value	Parameter	Value
a	6.53	α	90°
b	11.00	β	102.61°
c	7.35	γ	90°

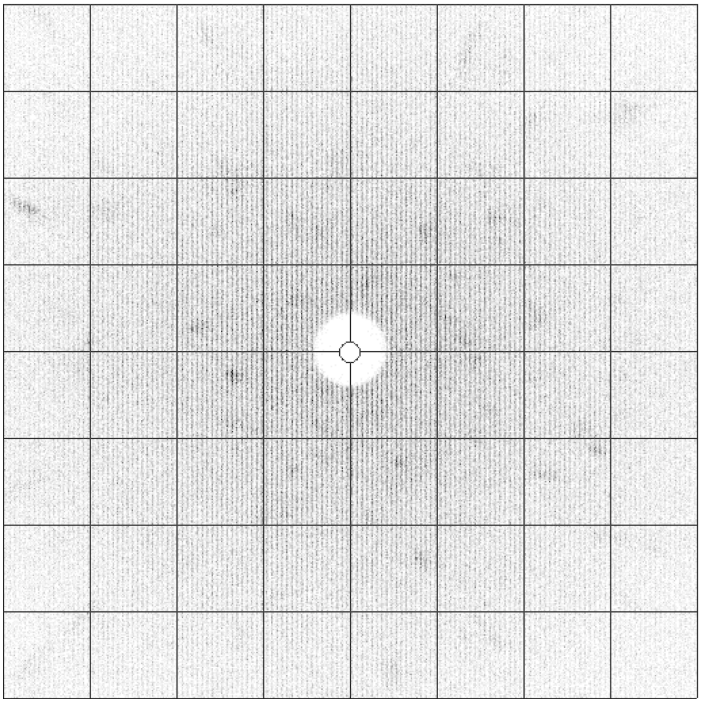

Figure 2.2. 2D diffraction pattern of HMX provided by Laue Back Reflection XRD for the sample in figure 3.15.

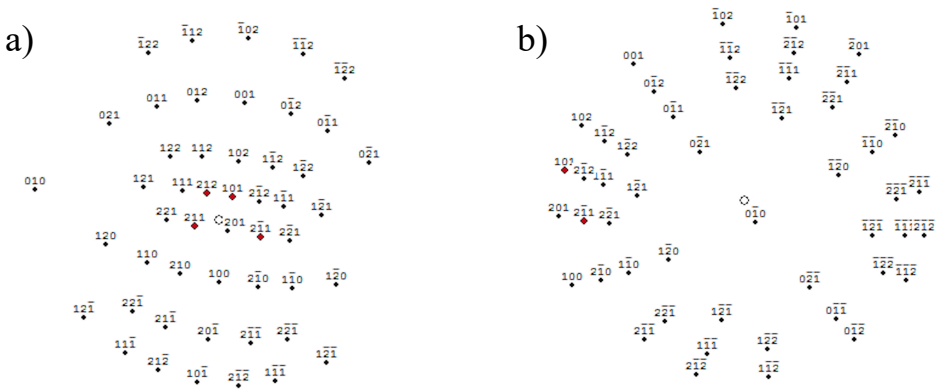

Figure 2.3. Stereographic Projection of HMX diffraction pattern at a) 0° (impacted plane) and b) 90° (viewed plane) for the sample in figure 3.15.

2.1.3 Engineered Defects

Many of the samples discussed here contain engineered defects that were added after the HMX crystals were recrystallized (and in the cases where Laue XRD was used, the defects were added later). The cylindrical holes were added to the samples using a micro drill press (Cameron Model 214-CS Table Top Drill Press). Several different drill bits (ranging from 100 to 500 μm) were used in the samples discussed here. An adhesive (water soluble and low melting-point) was used to hold the crystals on a mount for the drilling process. During drilling, the crystals were cooled with water to reduce cracking. Finally, the samples were hand lapped on two sides to improve surface quality. The milled slots were made in a similar fashion using the same setup (shown below). This time, the slot was milled across the top of the sample using a ball mill rather than drilling down into the sample. Two passes are made, the first at a shallow depth, the second at the full depth (80 or 100 μm). Again the crystals are water cooled during the process to avoid cracking.

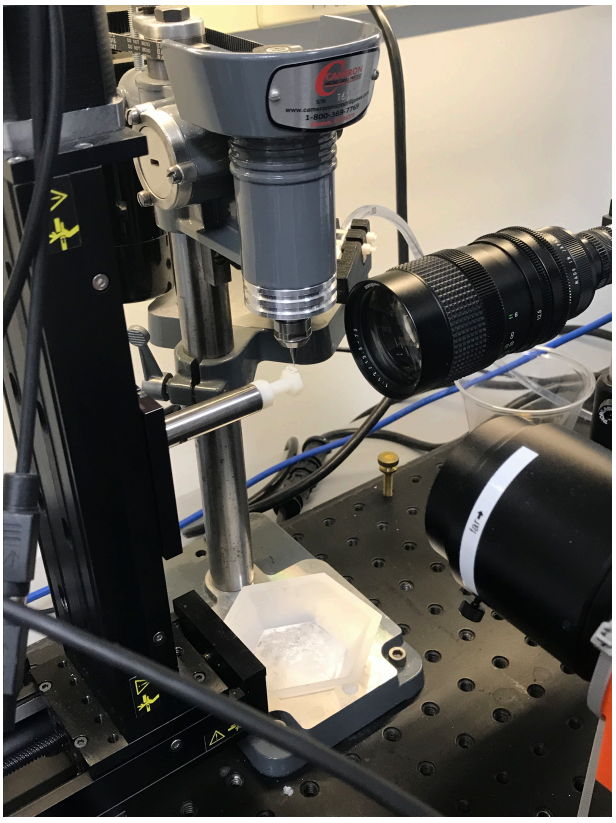

Figure 2.4. Drill press setup used to add engineered defects to HMX crystals.

2.1.4 Petri Dish Method

The original method for forming the PBX samples was the petri dish method. This provided a simple way to create a sample with multiple particles, however it provided little to no geometric repeatability. Only the first two samples described here were made with this method (the two samples containing more than two particles). First, a roughly 1 mm layer of Sylgard-184® was placed in the bottom of a Teflon® Petri Dish. After this layer was fully cured (30 minutes at 100°C), production grade HMX particles were placed in the desired geometry. After this, more Sylgard-184® was added to cover the samples and add an additional 1 mm layer over the top of the particles. Finally, this layer was cured and the sample was cut out of the petri dish to resemble the geometry shown below.

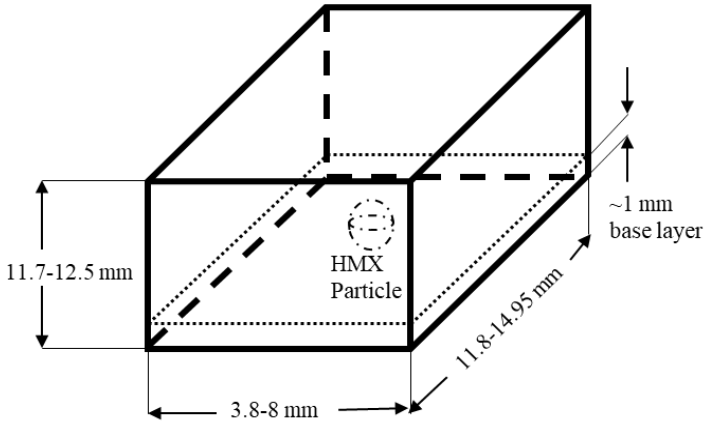

Figure 2.5. Schematic of sample made in petri dish [36].

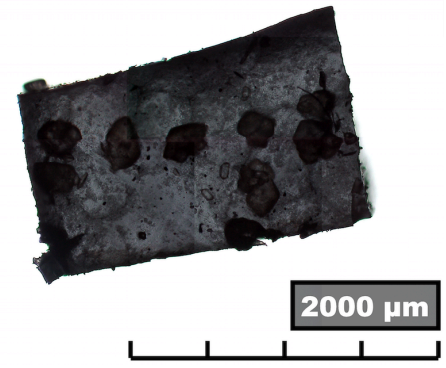

Figure 2.6. Multi-particle sample produced using the petri dish mold.

2.1.5 Rectangular Prism Mold Method

In order to increase the repeatability of the sample geometry, a Teflon® mold was machined and used for the three duo crystal samples discussed later on. A schematic of the mold can be seen below. Here, a raised platform was added so that the crystals could be placed in a precise orientation and held in place while the cavity around was filled with Sylgard-184® up to the top of the first crystal. This layer was partially cured (20 minutes) before the second crystal was placed on top of the other one and again held in place. Finally, the rest of the cavity was filled with Sylgard-184® and fully cured for 30 minutes. The final sample geometry was 10.2 mm square at the base and 15.2 mm in height (to mimic the petri dish sample sizes).

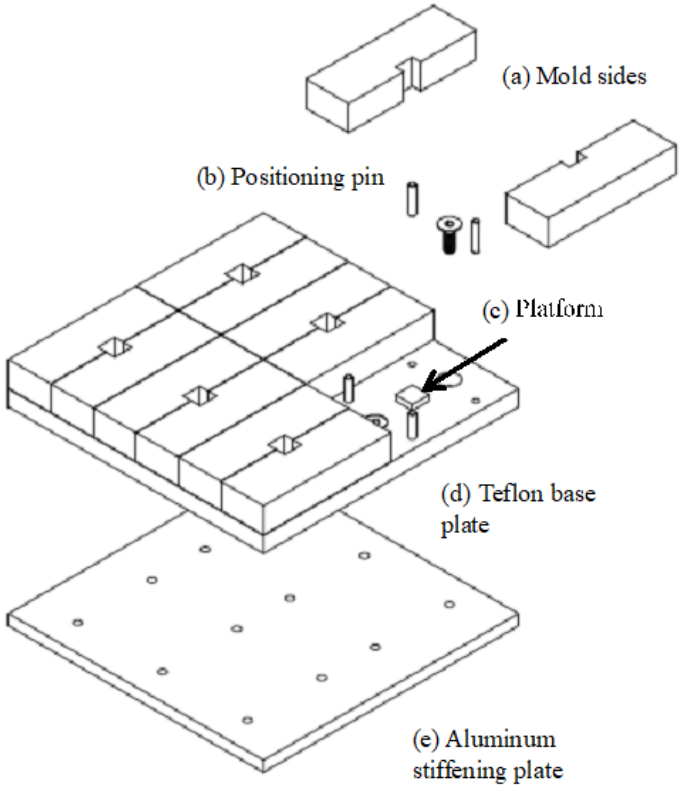

Figure 2.7. Exploded view of rectangular prism mold [36].

2.1.6 Pipet Method

Eventually the method was changed a final time to create a cylindrical geometry to simplify wave interactions. Furthermore, this method allowed flexibility in the placement of the samples and was very repeatable. This method was used for all of the engineered defect samples. To start, machined Teflon® rods formed the base of the sample. A very small amount of Sylgard-194® was placed on the rod and the HMX crystal was placed on top in the desired orientation. The rod was then placed in an oven at 100°C for about 10 minutes to cure the Sylgard-184® to a point that the crystal was firmly in place. Next, a plastic sheath, made from cutting the top and bottom of the bulb from a pipet, was placed over the rod to form an open-ended tube around the HMX crystal. This tube was then filled with Sylgard-184® (in some cases doped with the Fe_2O_3 as in figure 2.9) and placed in a vacuum chamber to remove the bubbles. After the bubbles had all risen to the surface, the sample was removed and placed in the vacuum oven for the full 30-minute cure. Next, the samples were removed from the rod and cut out of the plastic sheath. Finally, the top of the sample (which now has formed a meniscus) was cut to form a flat plane with the desired amount of Sylgard-184® in front of the sample.

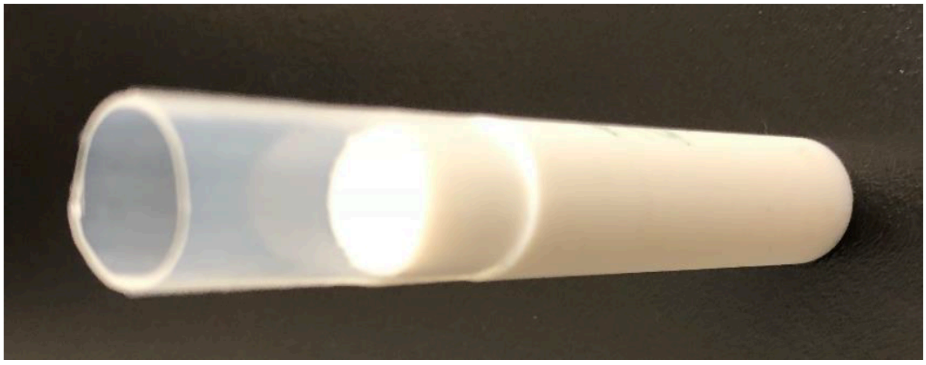

Figure 2.8. Teflon® rod with PE sheath (from pipet bulb) attached [36].

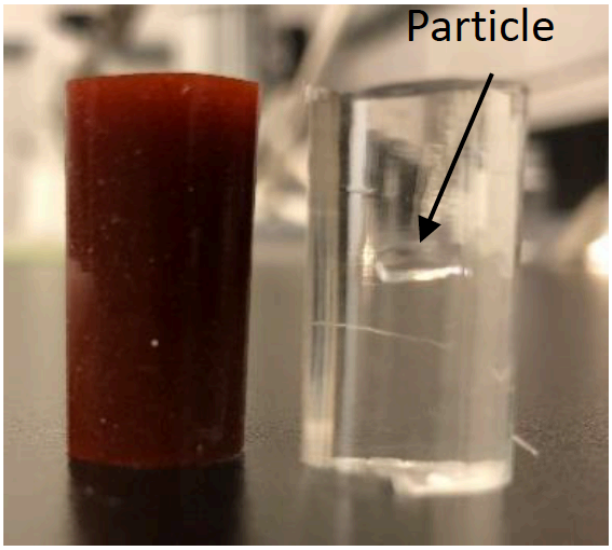

Figure 2.9. Pipet method samples: the sample on the left contains Fe_2O_3 thus is opaque while the sample on the right does not [36].

2.2 Experimental Method

Once the sample making process was completed, the first step in the experimental method was to take a 3D scan of the samples using X-ray tomography. Next, the samples were attached to a fixture and impacted with the gas gun. Finally, the images from the camera were compiled and analyzed.

2.2.1 Tomography

Many of the samples included in this work underwent 3D X-ray tomography before impact testing. This process provides a series of images that can be reconstructed to form a 3D stack of images of the sample, which allows for a realistic model to be constructed. These models can be used to predict what may occur under the impact conditions to compare with the PCI video. This process can be used to both aid in improving modeling techniques to reflect reality, and in some cases to better understand what is occurring in the original impacted sample. The tomography discussed here was performed at the Advanced Photon Source (APS) at Argonne National Laboratory at beamline 2-BM with a monochromatic 25 keV X-ray beam. The

samples are placed onto a magnetic stage (already in the Sylgard-184® matrix) vertically with the HMX crystal (back of the sample) at the top. The device rotates the stage 360° to provide a full view of the sample. After the scan is complete, the images need to be reconstructed using an in-house script that 2-BM provides. These reconstructed images are then combined in a stack using ImageJ and adjusted to provide the best contrast and brightness. One slice from an engineered defect sample can be seen below.

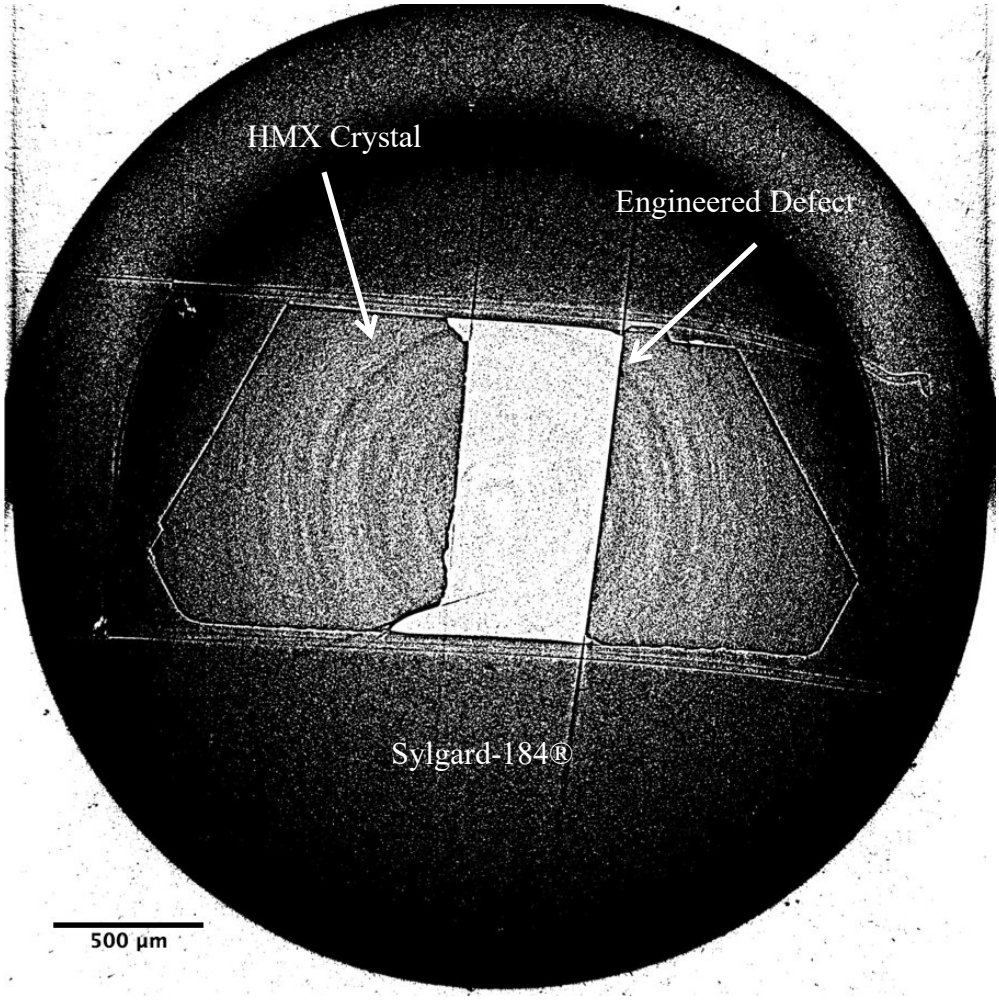

Figure 2.10. Single slice of the 3D tomography of the sample shown in figure 3.2.

2.2.2 Gas Gun Setup

The experimental work was performed using a gas gun with X-ray PCI to observe the dynamic deformation process in the sample as it was subjected to impact loading. The gas gun was a single stage, smoothbore, light gas gun with a barrel length of 1.83 m and bore diameter of 38.1 mm. At the time of these experiments, the maximum velocity of the gas gun was about 500 m/s. The impact event was captured using X-ray PCI provided at beamline 32-ID B at the APS at Argonne National Laboratory. The system allows the observation of phenomena not possible with standard optics due to the opaque nature of the samples, such as particle-matrix, and particle-particle interactions. X-rays pass into and out of the gun target chamber through a window to a scintillator placed in front of the camera lens, converting the X-rays to visible light [50]. Next, the light passes through an additional lens that magnifies the image (5x, or 10x) for better resolution. Finally, the light enters a Shimadzu HPV-X2 high-speed camera which records the impact event in real time at 5 million frames per second. The schematic for this setup is seen in figure 2.11. There are only two major differences in the setup between the various samples: the sabot and the triggering system. The samples containing more than two particle samples (only two discussed here) used a low-density polyurethane sabot formed in a cylindrical steel mold. A drill was used to bore out part of the center of the cylinder and an aluminum impactor was added. The remainder of the samples used a sabot that was machined out of Delrin® for precision and fitted with an aluminum (two crystal samples) or steel impactor (all others). This change was made to lower the tolerances on the sabot to allow for higher impact velocities. The triggering system also made a change between the groups of samples to precisely capture the impact event. For the samples containing more than two particles, a five-volt laser was used to trigger the camera. This laser was placed ~25 mm in front of the sample and a delay generator was used to ensure the camera captured the impact event. This setup functioned well at lower velocities, however the trigger became unreliable at higher velocities. Next, the experiments were triggered using shorting pins: two wires that completed a circuit when connected by the impactor. These would be placed just behind the face of the sample to ensure a clean contact with the sample surface. When connected, they would complete a capacitor circuit and trigger the camera. These worked well, but were eventually replaced with piezo-electric impact pins that operated with extremely high reliability (only one failure in over 50 experiments). These pins required no circuit, as they would provide signal on impact, triggering the camera. Additionally,

a second pin can be added a measured distance behind the first to provide a velocity measurement. The only additional change between experiments were slight variances in the delay settings for the camera and X-ray shutters as well as changes in the sample fixture. Throughout the study, an oscilloscope was used to find the function time (time between firing signal and camera trigger) to provide the best window for capturing the X-ray PCI images.

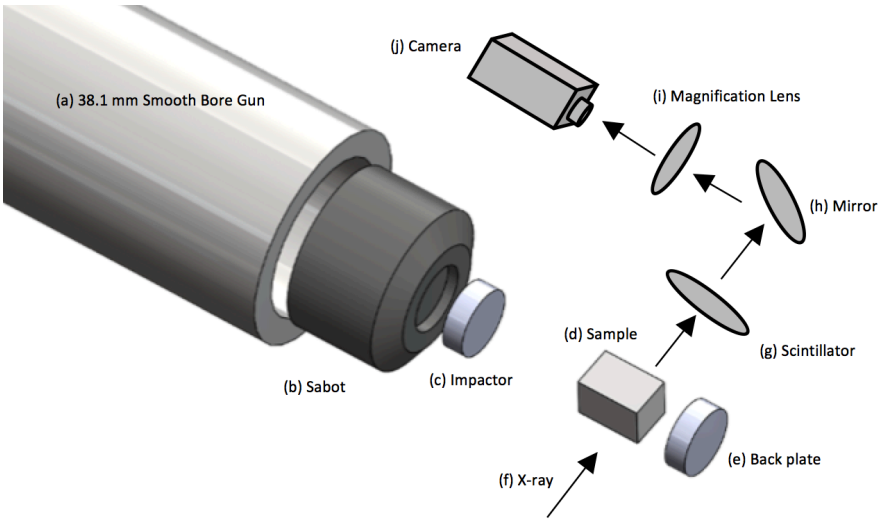

Figure 2.11. Gas gun setup schematic with X-ray imaging system.

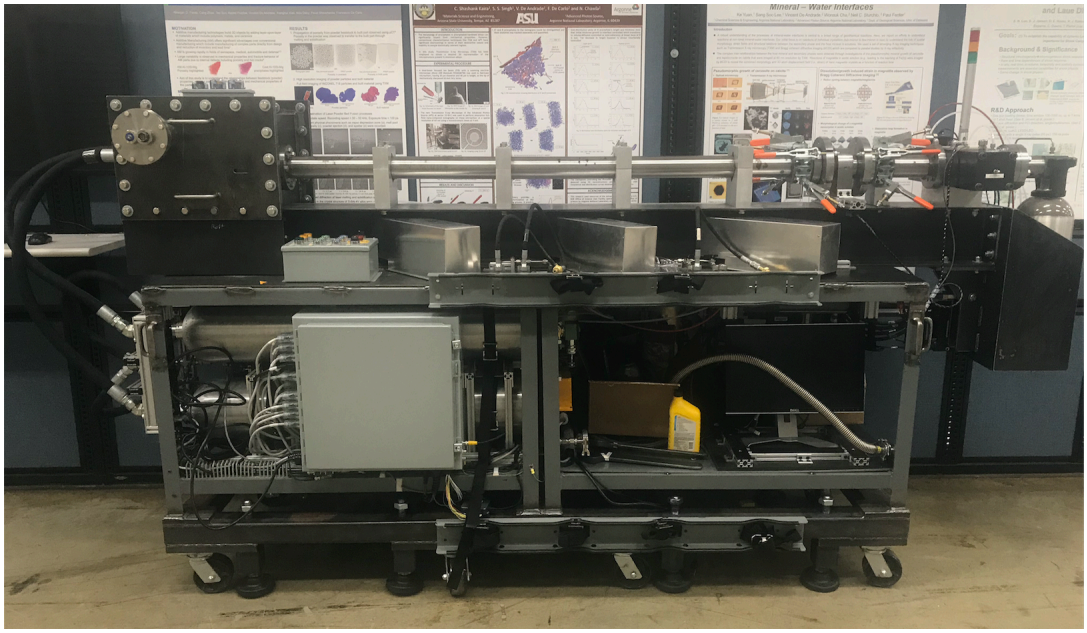

Figure 2.12. Photograph of the gas gun.

2.2.3 Sample Fixture

The sample fixture changed slightly between each cycle at 32-ID B in order to continually improve the data. The basic setup used can be seen below. The foundational piece of the fixture was a 0.2" thick Aluminum "X" with four holes on the corners to attach to the four bolts on the inside of the gas gun chamber. Next, a 3D printed (in most cases PLA) holder was bonded to the "X" with an adhesive. This piece provided a structure to hold the back plate (a steel/aluminum disc placed behind the sample) as well as the PBX sample in place. Finally, zip ties were used to place the triggering pins next to the sample. This entire setup was placed on the four bolts in the chamber with plastic spacers in front and a nut behind to hold the sample firmly in the viewing window. Over time, several small changes were made starting with a thicker "X." The thickness was increased to 0.5" (with notches to aid in fracture upon impact) in order to decrease the amount with which the fixture flexed upon impact. Next, some of the spacers were replaced with stiff springs in order to allow slight adjustments (pitch and yaw) particularly with the engineered defect samples (to position holes and slots in a perfect geometry: end on). Finally, the back plate was replaced with a steel insert that screwed on to the fixture allowing for a roll movement. These adjustments allowed for total control of the placement on the sample in the X-ray viewing window.

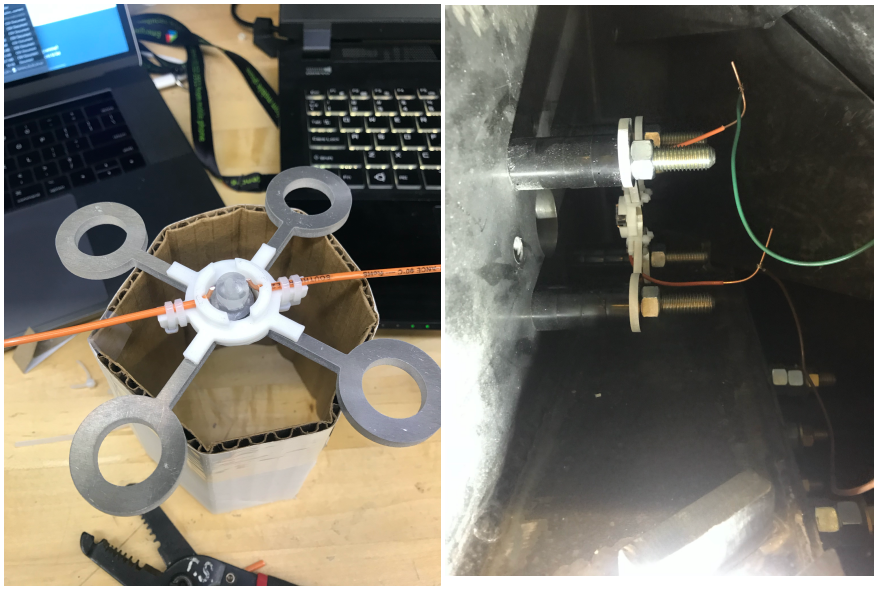

Figure 2.13. Original fixture setup with shorting pins. The left image shows the assembled fixture and the right shows the fixture in the gas gun chamber.

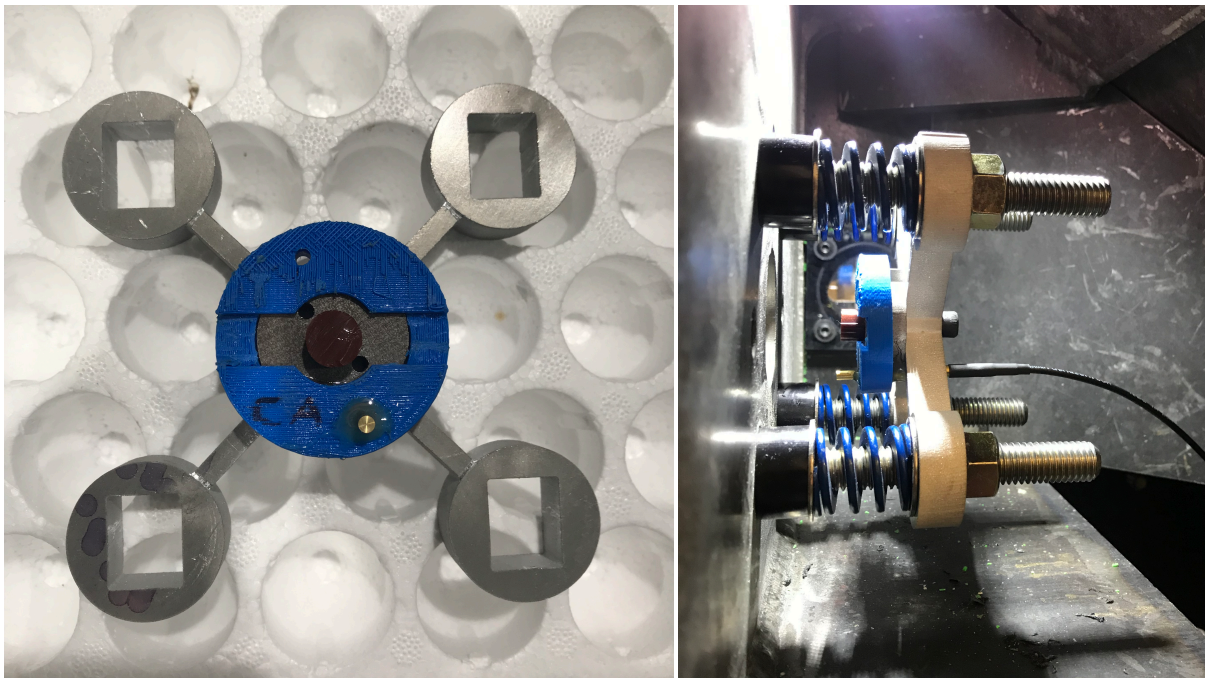

Figure 2.14. Improved fixture setup with piezoelectric pins. The left image shows the assembled fixture and the right shows the fixture in the gas gun chamber.

2.2.4 Data Analysis

During testing, a comprehensive spreadsheet was used to record any relevant data and observations including function time (time between firing signal and camera trigger), sabot mass, sample qualities, impactor/fixture type, undulator gap, any delay settings, and firing pressure. The camera software provides a video to view moments after impact which can be viewed to form initial observations, as well as to determine if adjustments need to be made before additional experiments. Later, these images (.tiff files) are loaded into ImageJ for analysis. First, the contrast and brightness are adjusted to best view the image. Next, a scale bar is added using the conversion of 6.4 pixels to 1 μm determined previously with a ruler in the viewing window. Then, several images are analyzed to find the sabot moving through the sample to determine the impact velocity (in some cases, two piezo-electric pins were used at two distances to estimate velocity but ultimately the video method appears to provide better results). Finally, these images are observed to determine what damage occurred in the sample.

3. RESULTS AND DISCUSSION

3.1 Multi-particle Samples

This section describes two different types of multi-particle samples: multi-particle and two single crystals. These multi-particle samples are of interest as stress concentration and frictional heating at the interfaces are considered possible sources of hot spot formation [1, 3, 8, 11-15]. As a reminder, it should be noted for all of the images that follow that X-ray PCI differs from a conventional X-ray image in that the measurement is a change in the X-ray phase due to the refractive index of the material, not attenuation of the X-ray [34]. The measurement of the X-ray phase is more sensitive to changes in density and thickness, allowing for better resolution of structural details in the material [50]. This makes PCI a great tool for observing cracks and opening interfaces in the HMX particles and crystals. These features appear lighter in color in the gray scale images as the X-rays encounter the less dense medium. PCI also results in a two dimensional image of a three dimensional object which can make the image difficult to interpret. It can be helpful to closely study the initial image (before impact) to note the changes as the impact loading occurs. These features are also better categorized when all of the images can be viewed together in sequence. Arrows have been added to help point out these features. It should be noted that while categorizing these opening interfaces is done with supporting evidence, the limitations of X-ray PCI prohibit these claims from being absolute.

The first two samples, figures 3.2 and 3.3, contain the production grade multi-particle samples. The initial frame in each figure shows the sample before impact, pointing out the placement of the particles. In figure 3.2 (420 m/s), the second frame (t = 5.0 μs) shows the initial damage that occurs when the compressive wave reaches the particles in the sample. A network of lighter colored lines form on each of the particles, indicating either cracking in the particles or open interfaces due to debonding with the matrix. These lines initially focus around the outer edge of the particles, but begin to spread inward. Some of the lines are curved, likely indicating the latter explanation, however many are straight and appear to be cracks in the HMX particles. The third frame (t = 6.5 μs) shows the maximum expansion of this network before the sabot enters the frame and removes the sample from the viewing window. By this point, the lines have opened further and spread throughout the full volume of each particle. This behavior is mirrored

in figure 3.3 (429 m/s): initial lighter lines appear at the edge of the particles upon impact (t = 4.0 μs) that spread and expand up until t = 8.0 μs. As the cracks and open interfaces expand, the total volume occupied by the particles increases allowing for the particles to interact with one another. This provides opportunity for additional stress concentrations as well as frictional heating, in addition to the potential for hot spots to form at crack tips.

The second set of samples contained two low defect HMX crystals laid out as in figure 3.1. These crystals were placed again at the rear of the sample with about 10 mm of matrix material between the front of the sample and the crystals. The crystals contain far fewer initial defects than the production crystals and are notably larger. As expected, these experiments displayed less apparent cracking than the production grade particles above, but still displayed evidence of damage, particularly at the crystal-crystal interface. In the same form as the multi-particle samples, each of these figures show a frame from directly before impact, another from when the compressive wave reaches the crystal, and a third from the maximum damage before the sample is removed from the viewing window. Figure 3.4 (443 m/s) shows the top portion of two crystals laid very closely together in the matrix with a thin line representing the interface between the crystals. Upon impact, straight light lines appear running from the bottom left to the top right, originating from the crystal-crystal interface. In the third frame, the lines have expanded further into each crystal, particularly the back (right) crystal. In the final frame, the top right corner of the back crystal separates, pointing to the conclusion that these light lines are cracks and not just open interfaces due to debonding. In addition, the interface between the two crystals expands slightly. Figure 3.5 (488 m/s) shows some similar effects, although requires more explanation. The two crystals can be clearly seen before impact, but the lack of contrast causes the front crystal to primarily disappear in subsequent frames. The only trace of the front crystal left in the second and third frames are a network of straight light lines extending into the crystal, likely cracks originating at the crystal-crystal interface as discussed with figure 3.4. The same crack network can be seen in the rear crystal, however when the reflected wave returns, the crystal appears to twist (t = 7.8 μs) and crack further before the sabot enters the frame. This reflected wave originates from stress wave that is reflected off the steel disk at the rear of the sample due to the impedance mismatch between the PBX and back plate. The twisting motion likely results from either non-planar contact between the back of the crystal and the steel back plate, or a non-planar initial impact.

Figure 3.6 exhibited slightly different behavior than the other two. The second image in the sequence (t = 4.6 μs) shows the initial light lines, but this time more prominent in the forward crystal and more severe. The lines however are not as linear as figures 3.4 and 3.5, pointing to possible opening interfaces due to debonding between the crystal and matrix. A potential explanation for this debonding can be seen in the third frame at t = 8.0 μs as a clear separation becomes apparent between the two crystals. This separation is more significant than that seen in other samples, and is likely not entirely caused by the reflected wave. The separation of the crystals at their interface has two additional explanations. First, the expansion may be caused by the rotation of the crystals since the forward plane of the first crystal was not completely flat (similar to figure 3.5, this time at the crystal-crystal interface rather than the back). The separation may also be caused by reaction in the HMX crystals causing an expansion. As the crystals primarily separate after impact, increased stress concentrations are likely more influential than any frictional heating in this sample type (versus samples with many more particles present).

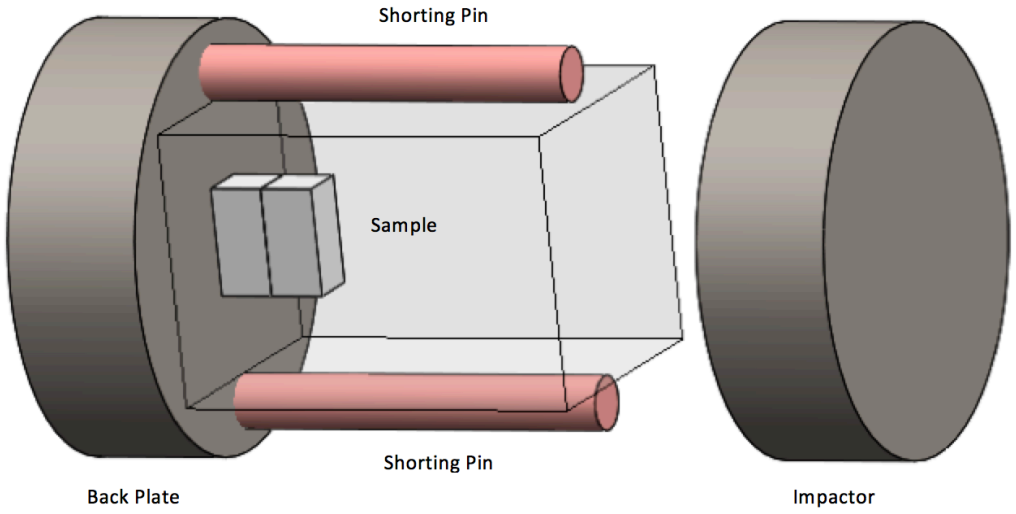

Figure 3.1. Schematic of two-crystal sample setup

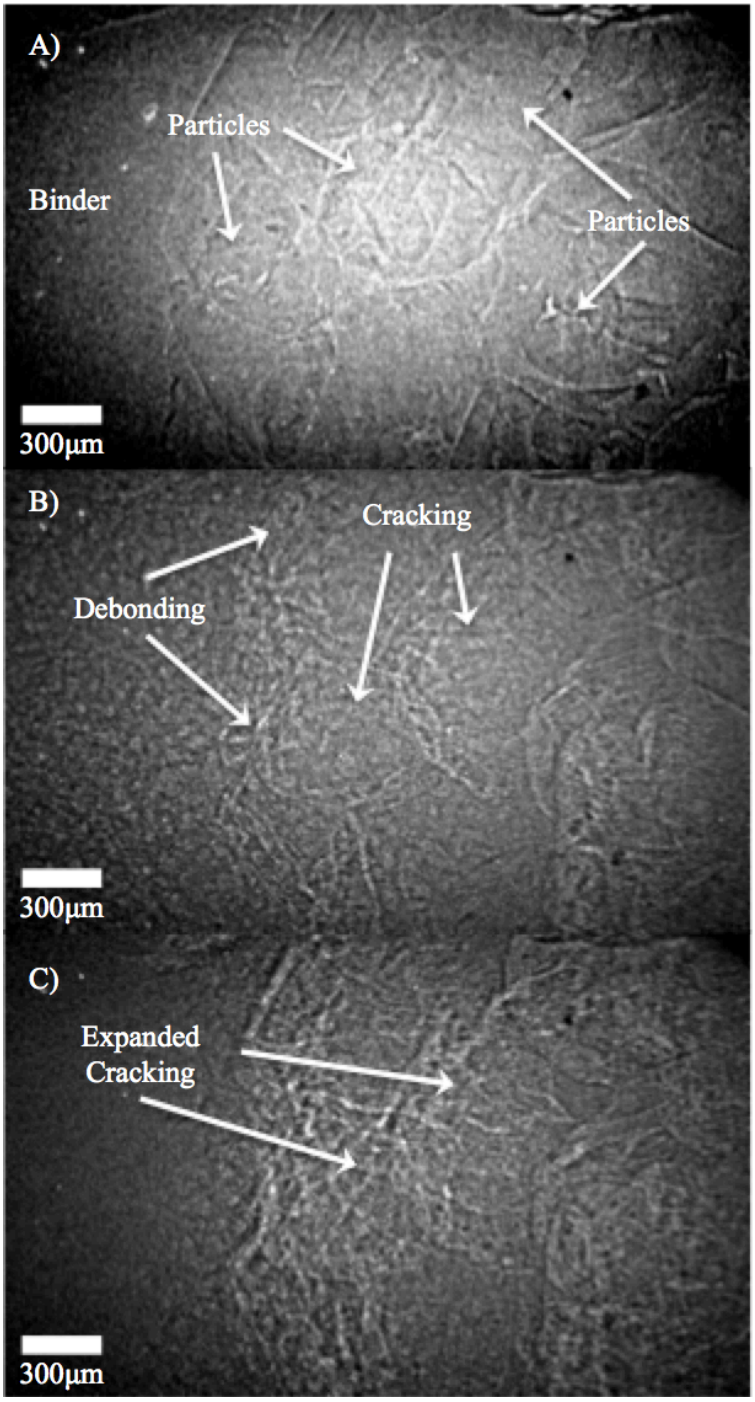

Figure 3.2. Image sequence of production HMX impacted at 420 m/s at A) 0 µs, B) 5.0 µs, and C) 6.5 µs.

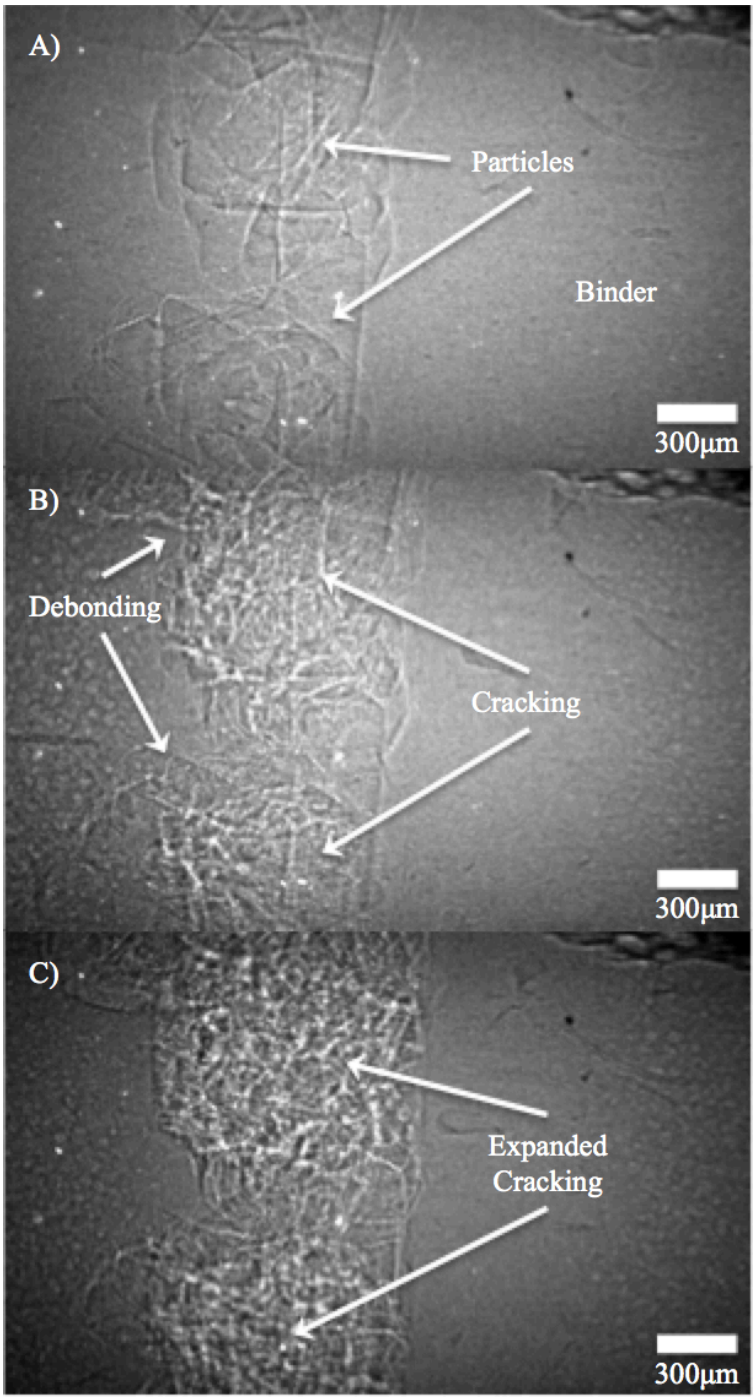

Figure 3.3. Image sequence of production HMX impacted at 429 m/s at A) 0 µs, B) 4.0 µs, and C) 8.5 µs.

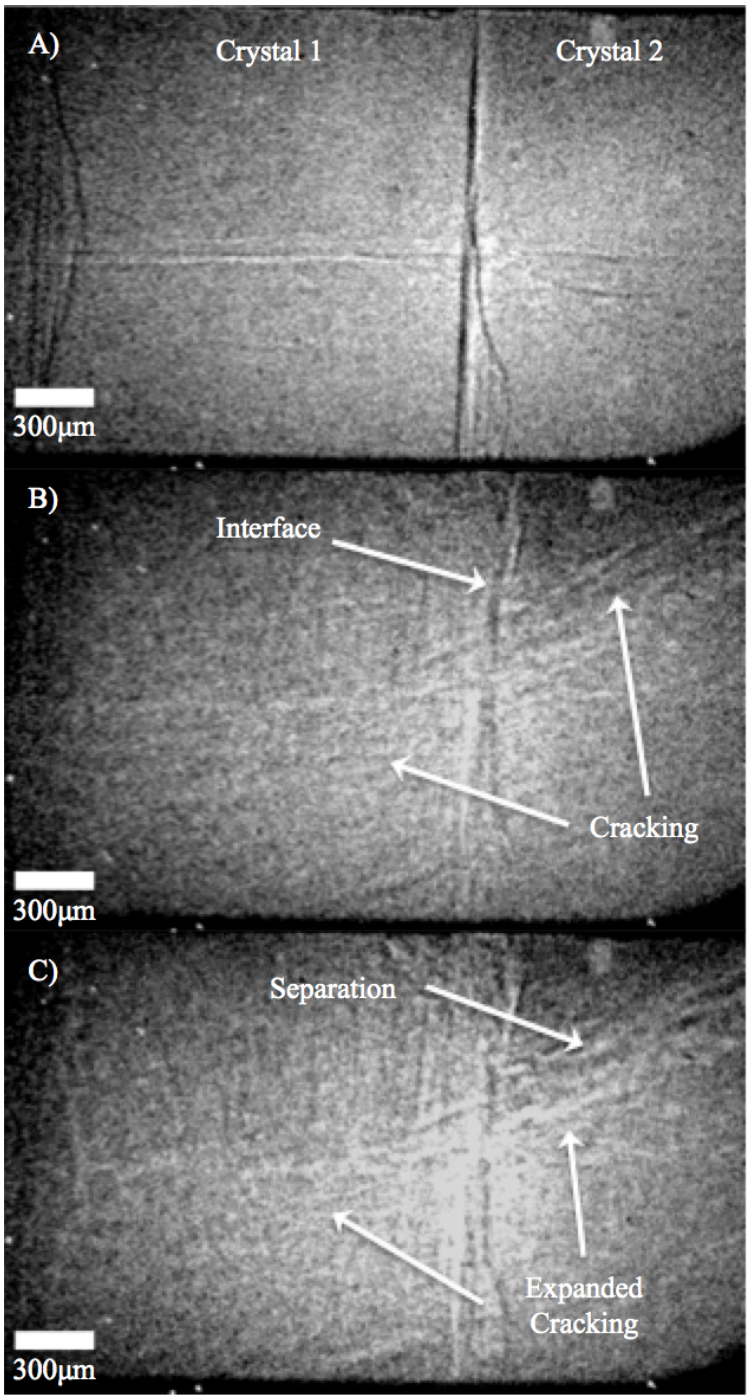

Figure 3.4. Image sequence of low defect HMX impacted at 443 m/s at A) 0 µs, B) 5.6 µs, and C) 9.0 µs.

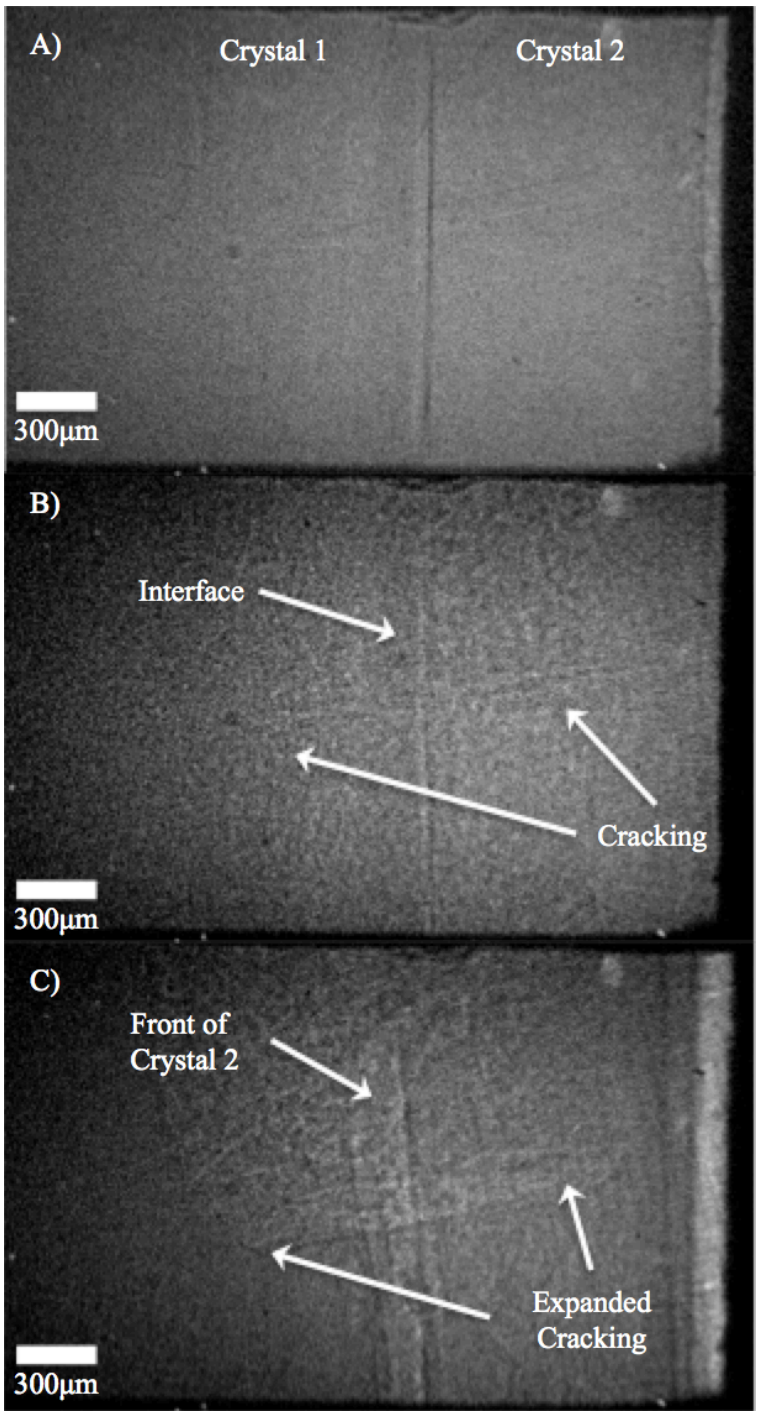

Figure 3.5. Image sequence of low defect HMX impacted at 488 m/s at A) 0 µs, B) 4.4 µs, and C) 7.8 µs.

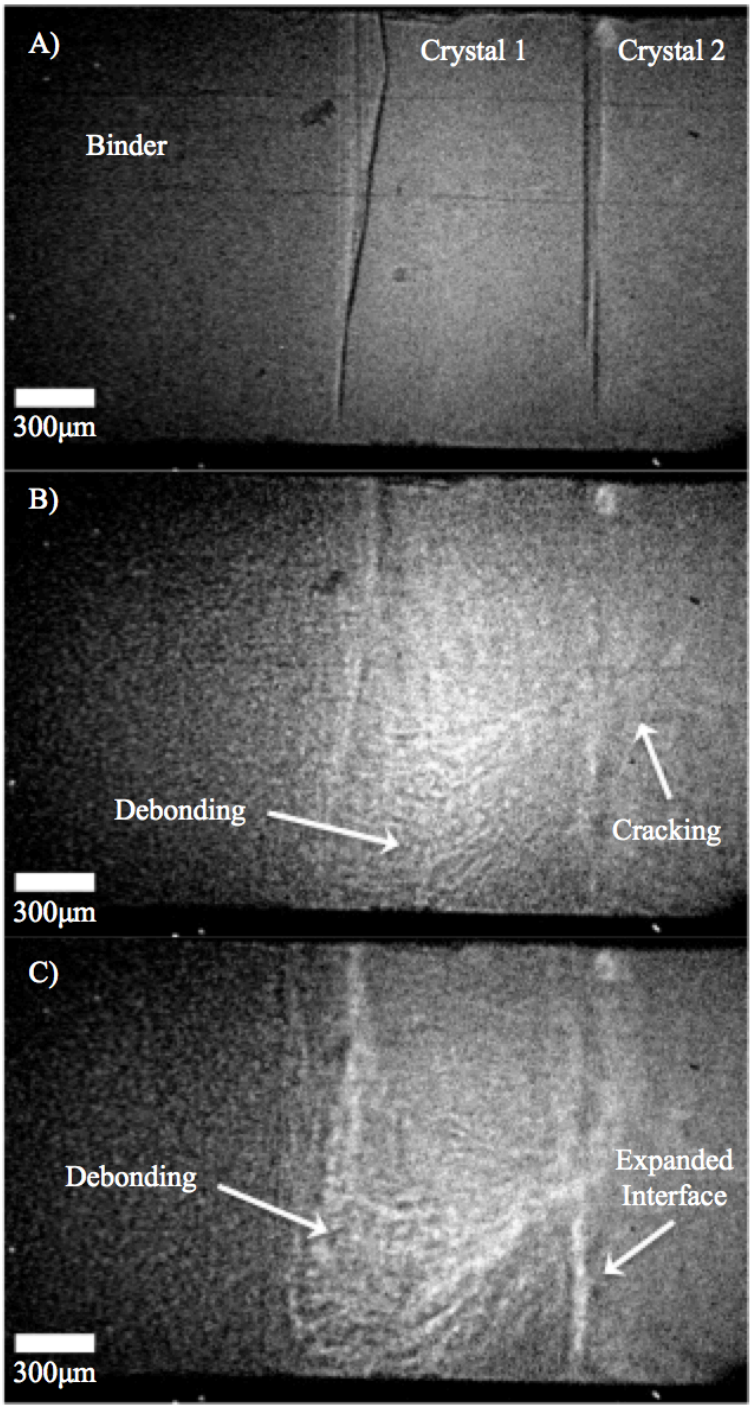

Figure 3.6. Image sequence of low defect HMX impacted at 432 m/s at A) 0 µs, B) 4.6 µs, and C) 8.0 µs.

3.2 Drilled Hole Samples

The next two sections will discuss samples containing engineered defect: defects added purposefully after the formation of the HMX crystal. First are the samples containing one or more drilled holes. These samples were designed to simulate the void collapse mechanism discussed in the introduction. Ideally, spherical voids would be added in the HMX, however there is not currently a method to add this type of defect. Instead, cylindrical holes are drilled into the sample as detailed in section 2.1.3 and viewed end-on (or as close as possible) to give the 2D representation of a circle (tomography of one such sample can be seen in figure 2.10). However, before looking at an end-on view, a sample containing a 500 μm drilled hole was impacted at 463 m/s where the hole was vertical to determine if the hole collapsed uniformly. This experiment is shown in figure 3.7 below. The first image shows the hole in a vertical fashion in the frame before the impact (noted t = 0 μs). At t = 0.4 μs the hole can be seen collapsing. The residual of the previous image (often referred to as "ghosting") provides an excellent frame of reference to observe how uniform the hole is collapsing in the vertical direction (normally "ghosting" is an issue which will be discussed further on in this section [34].) Here it can be seen that to start, the collapse is quite uniform as the new collapse line is nearly parallel to the original hole edge. At t = 1.2 μs, it can be seen that the line begins to break apart and is no longer completely parallel to the original hole (although it is still relatively uniform). Finally, at t = 1.8 μs (the final frame where the hole collapse is occurring) the line appears to be near parallel to the original hole edge, although not perfectly. This test shows that while the cylindrical hole is not a perfect analog for the ideal spherical void, the collapse is uniform enough to provide a good representation of how a pore would collapse at these conditions.

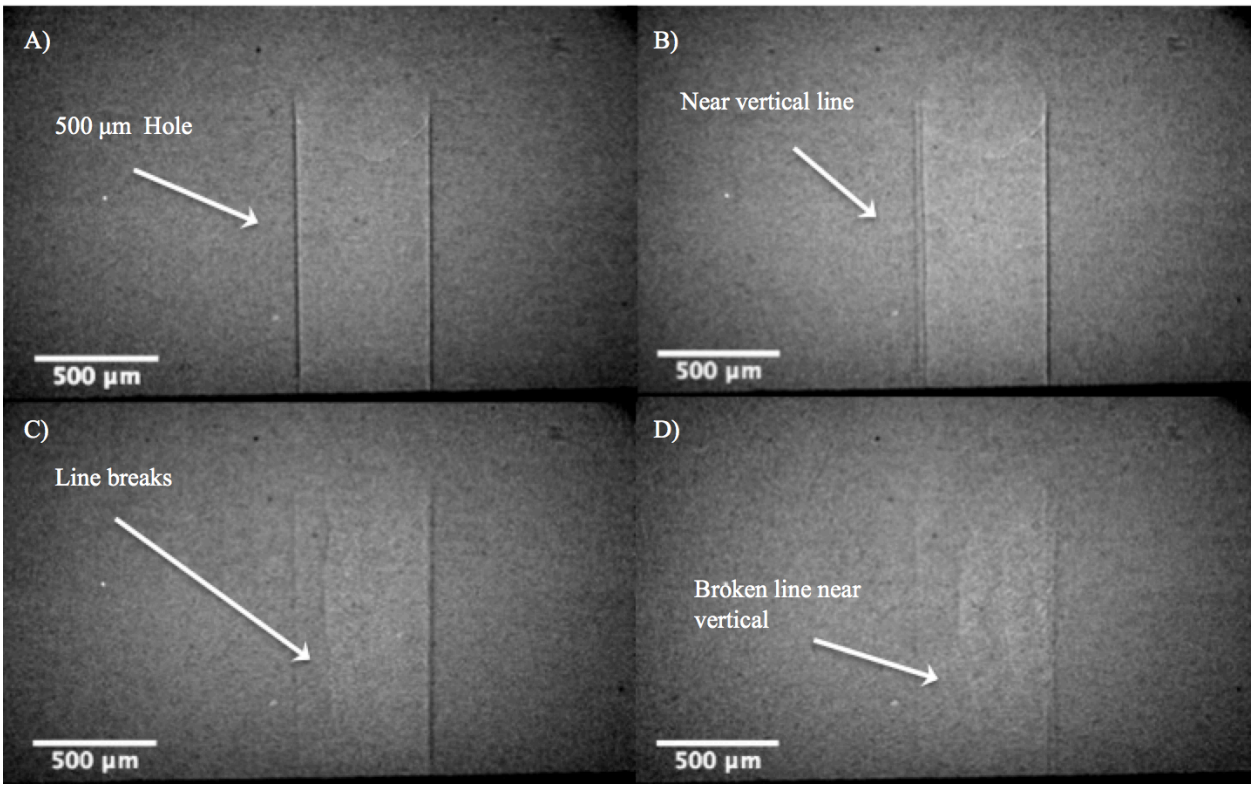

Figure 3.7. Image sequence of HMX containing a 500 µm hole impacted at 463 m/s at A) 0 µs, B) 0.4 µs, C) 1.2 µs, and D) 1.8 µs.

The next sample is an end on view of the 500 μm cylindrical hole at an impact velocity of 453 m/s. At this velocity, it is not expected that the collapse will result in liquid "jetting" or other specific hot-spot forming mechanisms, however the size of this hole provides a good opportunity to see how a pore collapses at this lower velocity as well as serves as a comparison point with computer models run on a similar sample [22]. A six image series of the pore collapse can be seen in figure 3.8 below. Also note that similar to the sample discussed previously, the normally problematic "ghosting" again provides a good frame of reference to the original hole (also the oval shape in the first frame is an air bubble in the Slygard-184® matrix, not an additional defect [34]).

At t = 0 μs, the end-on view of the hole can be seen the moment before impact. The next image at t = 0.4 μs shows the initial deformation that occurs on impact. This initial deformation appears uniform in reference to the original hole curvature. Next at t = 0.6 μs, the deformation follows in the uniform manner for the most part, however a small hook forms at the bottom of the collapsing hole. In the following frame at t = 0.8 μs, that hook becomes slightly more pronounced, but most of the collapse continues in the same uniform manner. Finally, in the last two images (t = 1.2 μs and t = 1.6 μs) the hook at the bottom becomes much more pronounced and it appears that the collapse moves further from the uniform manner towards a folding motion with a clockwise rotation. While this folding action is similar to the pore collapse seen in simulations at higher velocity where jetting may occur [1, 20-22], it is unlikely that a similar phenomena is occurring in this sample. At this velocity, cracking at the collapse boundary is likely and can be seen in the jagged nature of that boundary as the hook forms in figure 3.8. Furthermore, a similar jagged boundary can be seen in the later images of figure 3.7 discussed previously.

Using this sample to determine the impact conditions and sample dimensions, Duarte et al. simulated the potential pore collapse and sample response in a paper titled, "Void Collapse in Shocked β-HMX Single Crystals: Simulations and Experiments [23]." Here it was determined using impedance matching that the estimated particle velocity (u_p) for this sample setup would be 0.1 km/s. Using this, it was determined that stresses necessary for jetting would not be reached and the pore would collapse in a manner preserving the circular shape (as is seen for most of the collapse in figure 3.8) [23]. It should be noted that crystal orientation should have an effect and that information was not available at the time of this experiment [30].

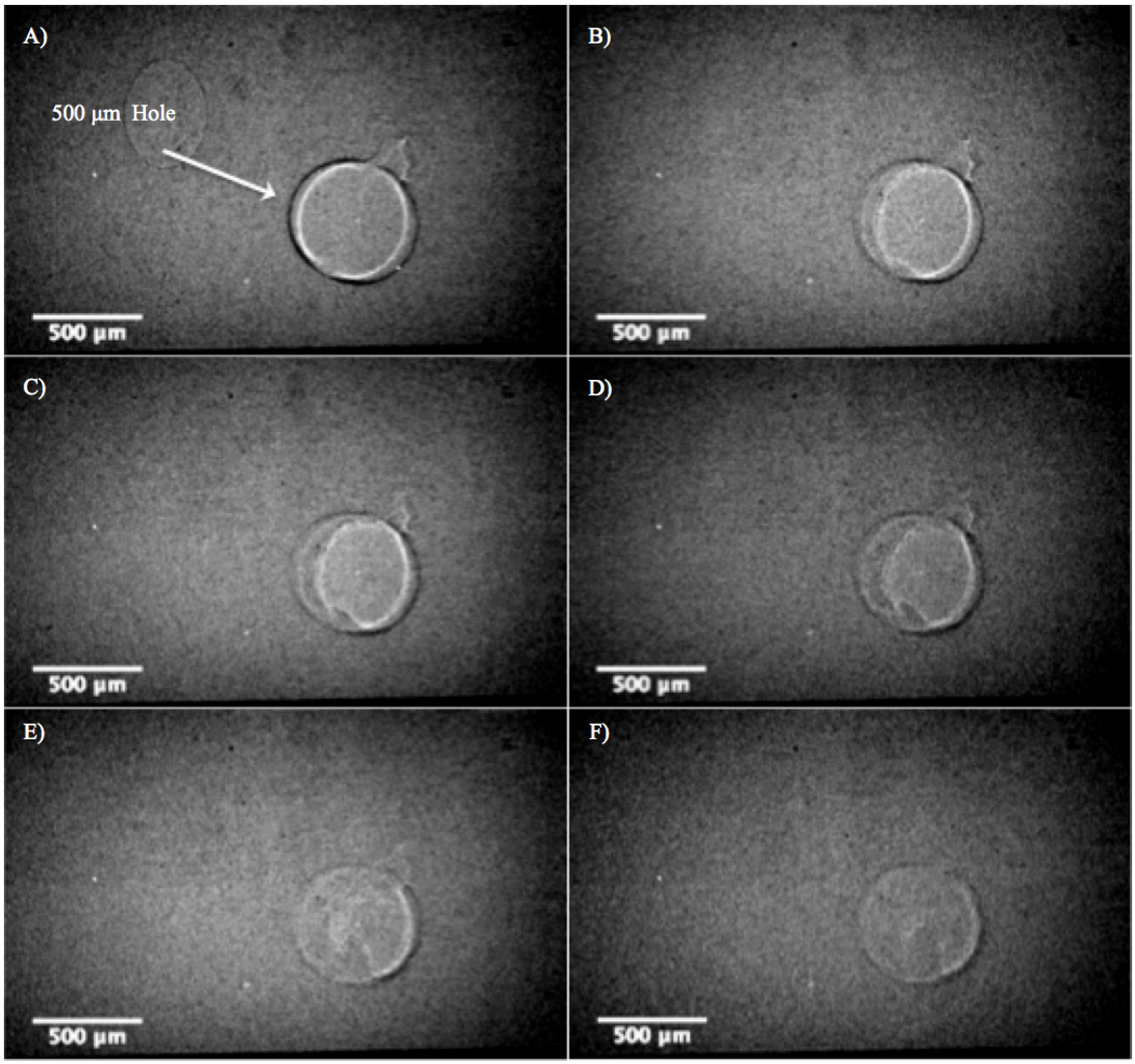

Figure 3.8. Image sequence of HMX containing a 500 µm hole impacted at 453 m/s at A) 0 µs, B) 0.4 µs, C) 0.6 µs, D) 0.8 µs, E) 1.2 µs, and F) 1.6 µs.

The next set of samples discussed here contain two 100 μm holes instead of one. The focus here is on the damage that occurs behind the hole rather than the shape of the hole collapse. As discussed in section 3.1, the lighter colors that appear in the gray scale images correspond to cracking or opening interfaces. The first of these samples can be seen in figure 3.9 and contains to holes in-line with the impact direction. The first frame shows the two holes (viewed at a slight angle about the x-axis) as well as the Sylgad-184® - HMX interface at t = 0 μs (the time in the lower left corner refers to the time since the trigger event occurred and can be ignored). At t = 0.8 μs, cracks can be seen forming at the rear of the holes after the hole collapse (here ghosting begins to present an issue as the holes have collapsed by this frame). These cracks continue to expand at t = 2.4 μs radially to the right (in the impact direction) from a larger vertical crack that forms in both crack systems. In the final image at t = 3.6 μs, the cracks extend to the largest point before the sabot enters the frame and clears the viewing window. At this point, cracks can be seen starting to spread to the left originating from the large vertical cracks. Here, the cracks originating from the front hole appear to be slightly larger which could be seen as confirmation of the shielding phenomena discussed by Kapahi (using damage as an indicator of temperature spikes at higher velocities), however this may simply be due to the fact that the shock wave reaches the front hole slightly before the back hole, giving the crack network more time to grow [21].

The next sample can be seen in figure 3.10 and shows a similar setup, yet this time with the two holes at a 45° angle (another system explored by Kapahi [21]). At t = 0 μs, the two holes can be seen viewed from a slight angle about the y-axis just before the shock wave reaches the holes. Next, at t = 1.2 μs, small horizontal cracks can be seen forming behind the collapsed holes. These cracks appear more linear than those found in the second image of figure 3.9, possibly due to a difference in the crystal orientation (while these sets of holes were drilled in what appeared to be different planes, the Laue XRD was not yet available to confirm this). The third image jumps to t = 3.2 μs after the two horizontal cracks migrate to the left before opening into a larger network. Finally, at t = 4.8 μs the two crack networks reach their full expansion before the viewing window is cleared. At this point, the front crack network again appears slightly larger than the rear network (this time in conflict with Kapahi) suggesting that the difference in the damage for both samples discussed here is primarily due to the total time the crack network has to form between impact and when the viewing window is cleared [21].

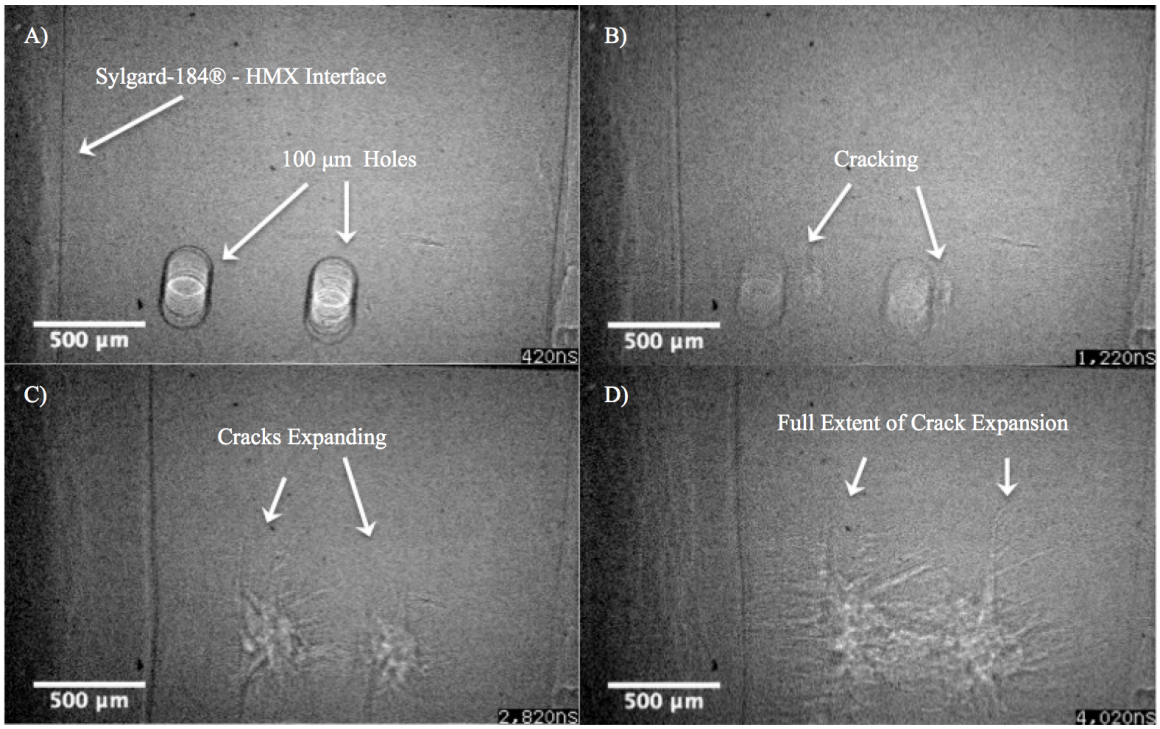

Figure 3.9. Image sequence of HMX containing two 100 µm holes impacted at 370 m/s at A) 0 µs, B) 0.8 µs, C) 2.4 µs, and D) 3.6 µs.

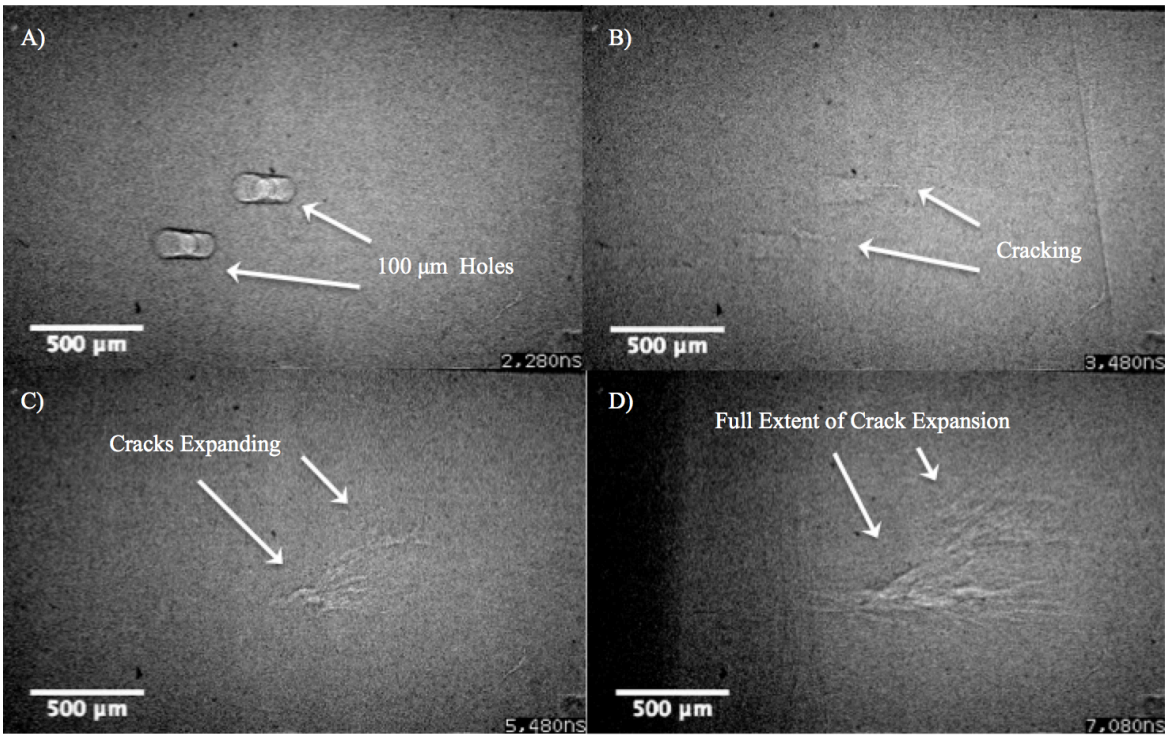

Figure 3.10. Image sequence of HMX containing two 100 µm holes impacted at 520 m/s at A) 0 µs, B) 1.2 µs, C) 3.2 µs, and D) 4.8 µs.

Before finishing this section, one additional sample will be looked at to discuss a possible issue in analyzing the two previous samples. These HMX crystals containing the holes are contained in a Sylgard-184® matrix where the hole opens directly into the matrix: as can be seen in the tomography (figure 2.10 in section 2.2.1). Also note that the hole is of a much lighter color than that of the polymer matrix in the tomography leading to the conclusion that the Sylgard-184® does not enter the hole, leaving only air. With this in mind, it has been discussed that the cracking that appears behind the pore collapse is not in the HMX, but in the polymer matrix due to the displaced air from the pore collapse. In order to completely rule this out, a similar sample will need to be impacted in a vacuum environment where the air has been removed from the holes. This capability will be available in the near future, however in the meantime a bare HMX sample was impacted containing two holes to see if similar cracking would be observed. The issue with this approach is that the lack of polymer in front of the crystal provides only a few frames to view the response before the viewing window is cleared. (Also, the PCI from this sample shows severe ghosting that will need to be addressed in the future.)

Figure 3.11 shows a bare HMX crystal containing two 200 μm holes, this time in a vertical alignment. This sample was also tested with the new fixture setup discussed in section 2.2.3 allowing for a near perfect end-on view (this should be the case for all future experiments). The second image (t = 0.6 μs) shows the first sign of cracking at the rear of the holes, similar to the second image in both figures 3.9 and 3.10. At t = 1.2 μs it appears that these cracks have expanded slightly and at t = 2.0 μs the cracks have migrated to the right slightly. While this is the extent of the cracking that can be seen before the viewing window is cleared, they seem to behave in a similar to figures 3.9 and 3.10. Again, future tests in a vacuum chamber should eliminate (or possibly confirm) these concerns, but the bare crystal test seems to corroborate the results found with the crystals in Sylgard-184®.

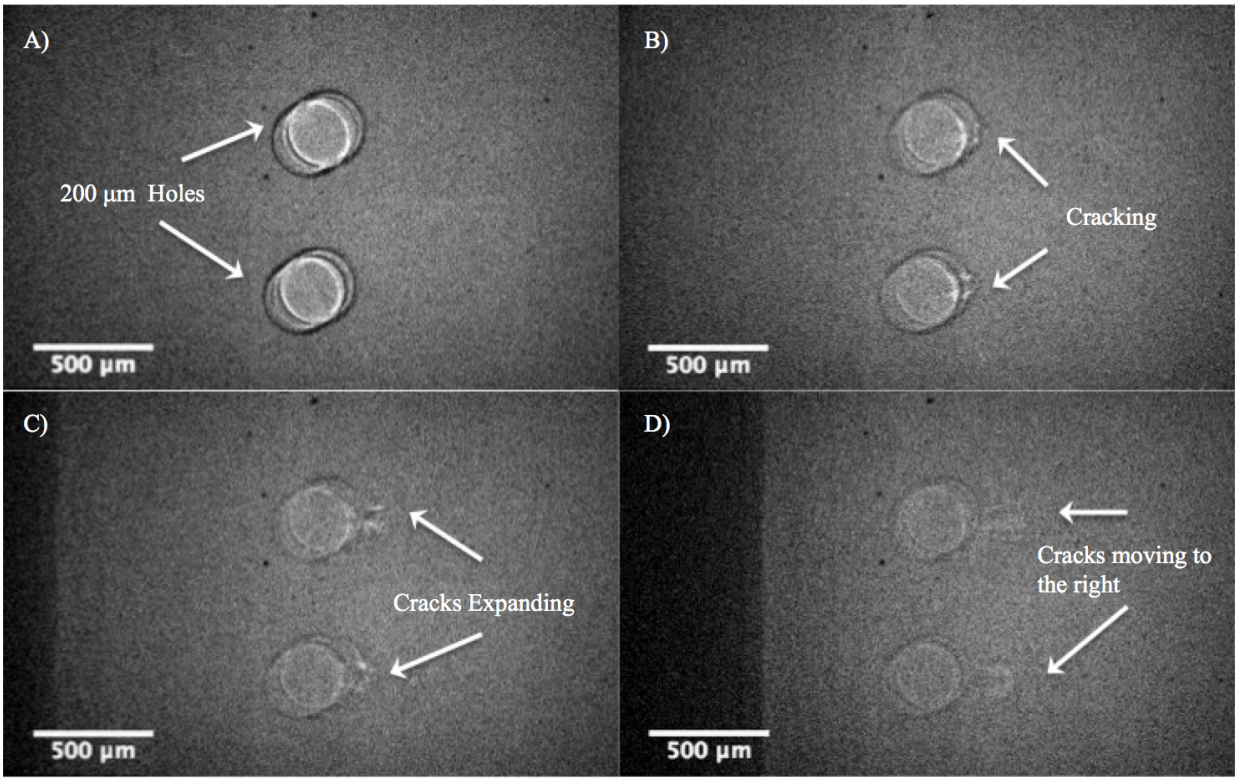

Figure 3.11. Image sequence of HMX containing two 200 µm holes impacted at 472 m/s at A) 0 µs, B) 0.6 µs, C) 1.2 µs, and D) 2.0 µs.

3.3 Milled Slot Samples

This section will detail the final subset of samples: the milled slot engineered defect. These samples were designed to show what increased damage may occur when initial cracks are added to the HMX (similar to the work done by Tanasoui and Daurte discussed in the introduction [23, 27]). It was determined that the best way to add a repeatable crack defect to the sample was to mill a slot across the face of the HMX crystal, as can be seen in figure 3.12. One limitation of PCI not yet discussed is the inability to determine which face of the crystal is facing the camera. Both the face away from the camera and towards it will appear the same in the image, providing a particular challenge in viewing this sample type. Over the course of these experiments, the improvements to the fixture setup discussed in section 2.2.3 improved the viewing angle of the slots, but they can still be difficult to make out. With this in mind, the slots are pointed out in the initial frame of each figure. The measurement listed with the slot is both the diameter of the ball used to mill the defect and the depth of the slot.

Figure 3.13 shows one of the first milled slot samples impacted, this one at 458 m/s. Due to the original fixture system, the 100 μm slot is shown at an angle along the front face in the first image at t = 0 μs. The second image shows the crystal at t = 1.8 μs after the shock wave compresses the sample the left. The crystal remains in this position until t = 3.0 μs when cracking starts to occur surrounding the position of the initial milled slot. The results to this point are as expected to this point, but at t = 4.2 μs angled lines rapidly form in a crisscrossing pattern in the crystal. These lines remain in the crystal through the next image at t = 5.6 μs before disappearing. Finally, at t = 7.4 μs the crystal can be seen breaking apart where the initial milled slot was located before the sabot clears the viewing window.

Both the pattern and shade of these angled lines are different than any other sample tested in this work. First, the patterns of the lines are uniform with all the lines running one of two directions (bottom left to top right or top left to bottom right). Next, as mentioned in section 3.1, when analyzing PCI images open interfaces appear lighter than the surroundings. In all other samples discussed here, cracks appear lighter because they are creating open interfaces within the crystal. Here the lines are darker than the surroundings similar to the edges of the crystal.
If the cracks were to remain closed, they may appear as darker lines (a closed interface such as the boundary of the crystal). The timing of these lines corresponds to the timing of the reflected wave resulting from the steel back plate so the sample is being compressed from both sides. In

other cases (such as with the sample shown in figure 3.6) these cracks expand under these conditions, although it is possible that the expansion is due to reaction in the crystal for those samples. Furthermore, this behavior may be dependent on the crystal orientation of the impacted plane. As with all samples discussed thus far, the crystal orientation is not known although educated guesses can be made from shape of the crystals (as they are grown in the same direction). Much effort was taken to reproduce the effects seen in this sample but that has yet to occur. The other milled slot samples result interesting cracking behavior that will be discussed next.

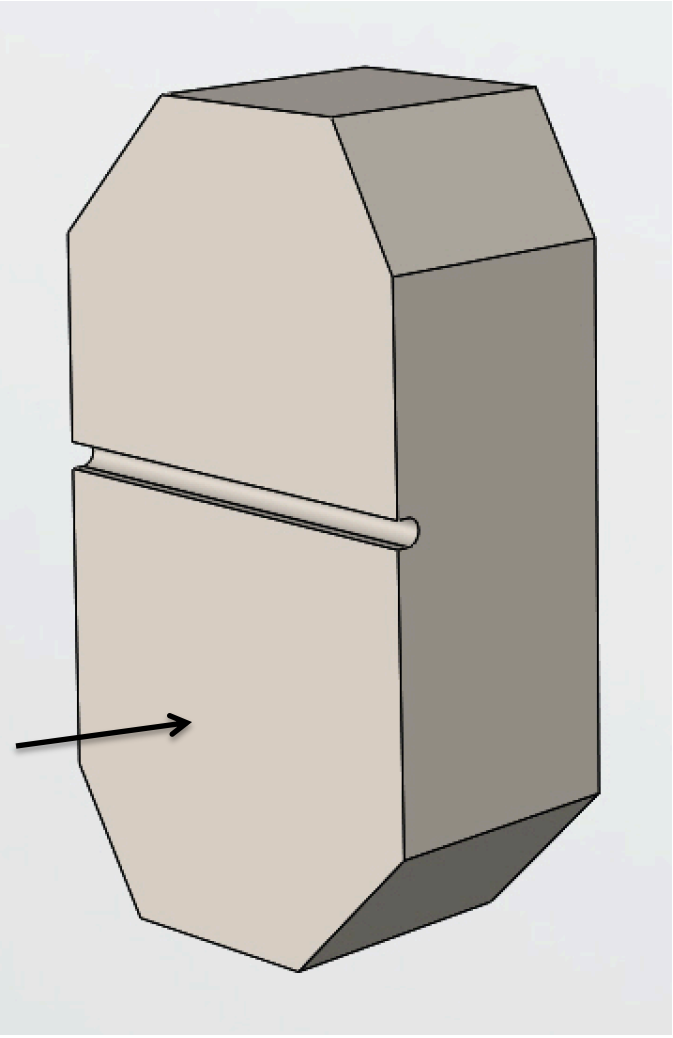

Figure 3.12. Schematic of a milled slot sample to be impacted on the front face.

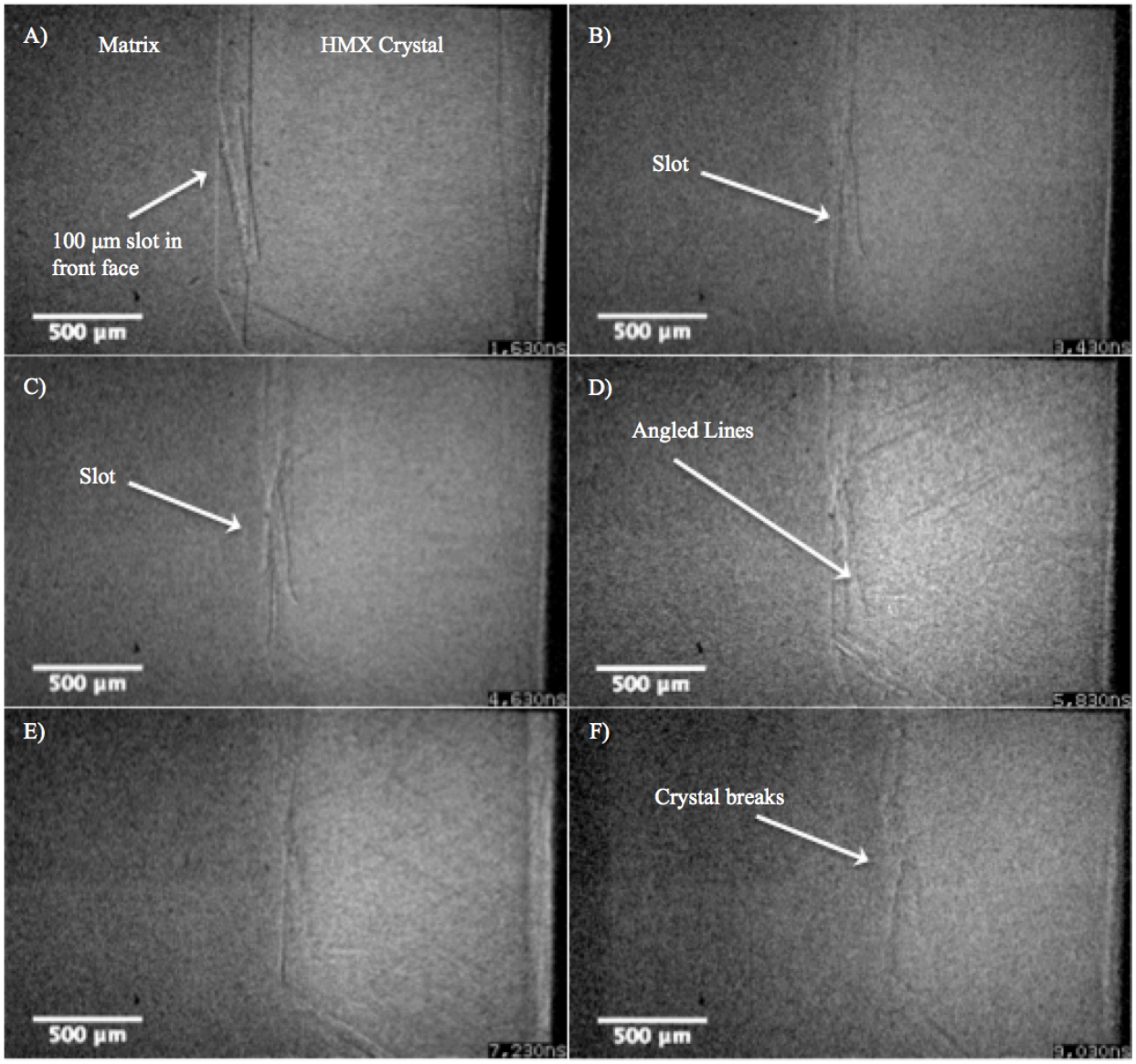

Figure 3.13. Image sequence of HMX containing a 100 µm milled slot impacted at 458 m/s at A) 0 µs, B) 1.8 µs, C) 3.0 µs, D) 4.2 µs, E) 5.6 µs, and F) 7.4 µs.

After redesigning the fixture system, another set of samples were tested in the same setup as figure 3.13. These samples did not show the same angled lines, but instead showed distinct cracking where the initial slot was added. Figure 3.14 details one such test with an 80 μm slot impacted at 439 m/s. This experiment took place during the same testing cycle as figure 3.11 thus deals with the same severe "ghosting." The second frame points out this residual image as well as extent of the deformation that occurs during the initial compression of the sample which occurs at t = 2.0 μs. At t = 4.0 μs distinct cracking occurs at the location of the milled slot. This crack network expands until t = 4.8 μs when the sabot clears the viewing window. While these events can be seen more clearly in the full PCI video, Fe_2O_3 particles were added back into the matrix for the final two samples to increase the contrast (these were removed in order to better position the samples with the clear polymer).

Figure 3.15 shows one of these samples containing a 100 μm slot impacted at 490 m/s. A few things of note can be seen in the initial image. First, there appears to be damage within the crystal noted by the lines (primarily vertical) running through the HMX crystal. These cracks likely occurred during the milling process, but may have been present before (as these cracks do not appear in the previous samples). While these cracks detract from the simplicity of the defect setup (one controlled slot), they do actually provide a more realistic situation presented by cracks in energetics contained in PBXs (similar to the Duarte work presented in the introduction [28]). Second, the light colored region with bubbles that appears to left is the adhesive binding the sample to the back plate. Normally this region cannot be seen, but the adhesive layer was thicker than normal in this sample. The second image at t = 3.0 μs again shows the furthest initial compression of the sample although this time it can be seen that the slot flattens during the compression. At t = 5.2 μs, cracks begin to appear largely running horizontal (left to right) across the crystal. The most prominent crack appears where the initial slot defect was added. Finally at t = 6.4 μs the cracks reach their full extent, again with the most prominent crack located where the slot defect was added. Also at this point, the rear of the crystal can be seen moving to the left (against the impact direction) as the reflected wave came from the steel backing plate.

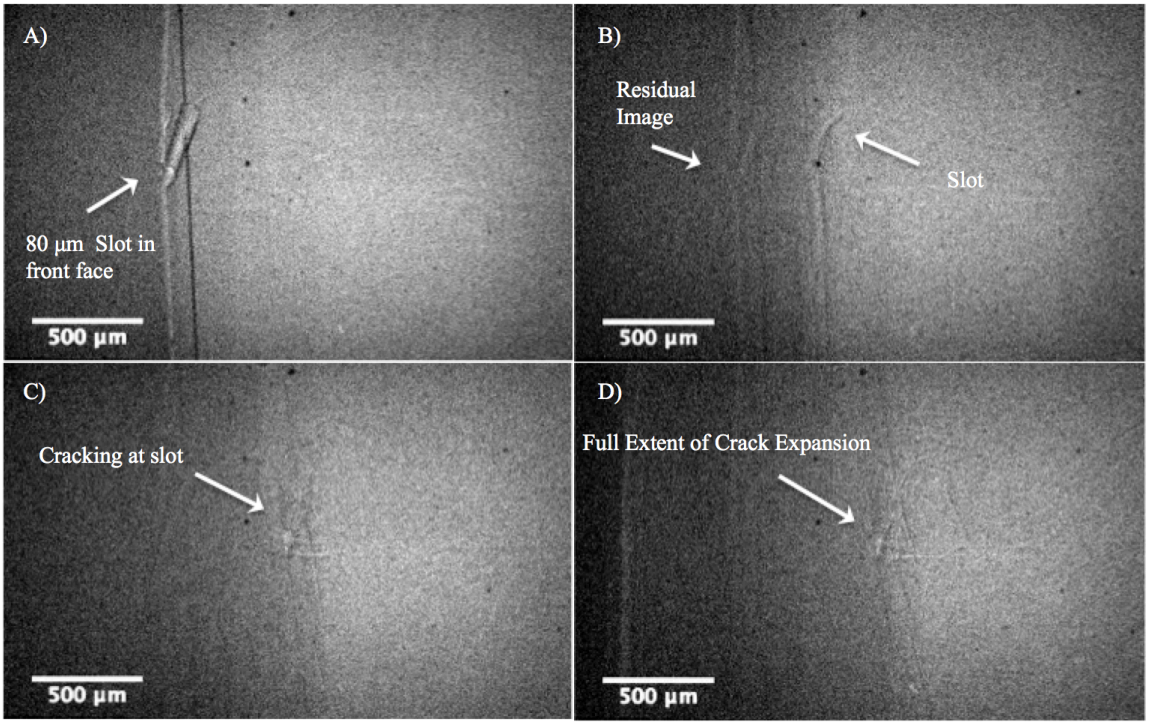

Figure 3.14. Image sequence of HMX containing an 80 µm milled slot impacted at 439 m/s at A) 0 µs, B) 2.0 µs, C) 4.0 µs, and D) 4.8 µs.

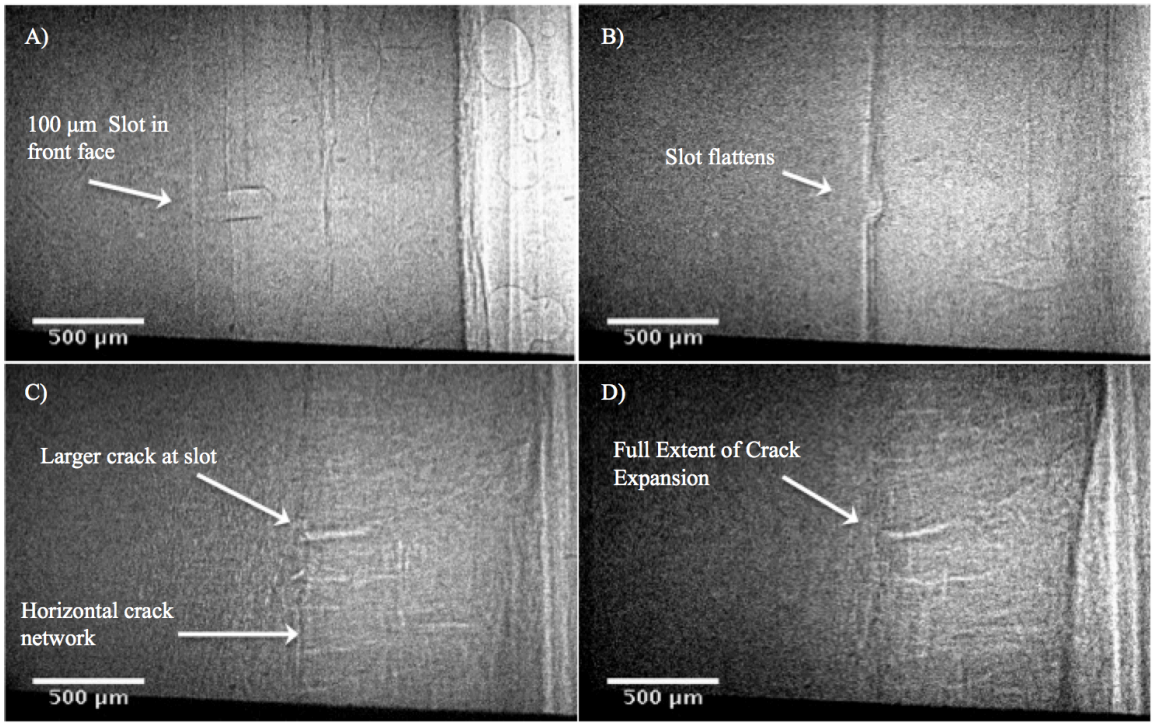

Figure 3.15. Image sequence of HMX containing a 100 µm milled slot impacted at 490 m/s at A) 0 µs, B) 3.0 µs, C) 5.2 µs, and D) 6.4 µs.

The final slot sample is the only sample discussed in this thesis that underwent Laue Back Reflection XRD (discussed in section 2.1.2). This method should be capable of defining the crystal plane in the HMX that is impacted. As discussed previously, the crystal structure of HMX along with the surface quality of the samples makes it difficult to exactly define the crystal plane. Further work will be needed to refine the data and provide more confidence in the reported plane. With these stipulations in place, the data points to the impact plane of this crystal to be the (201) plane and when rotated 90° the viewing plane (that is the plane of the PCI image) is very near the (0-10) plane (the diffraction pattern and the stereographic projections can be seen in figures 2.2 and 2.3).

Figure 3.16 shows this sample with a 100 μm slot impacted at 427 m/s. Note that the additional dark line in the first frame is not an internal crack as in figure 3.15 as it does not move throughout the impact event. This crack is outside of the sample, likely a defect in the scintillator. Just as with the sample in figure 3.15, with the initial compression (occurring until t = 4.2 μs) the slot flattens. Later at t = 6.6 μs cracks begin to form across the HMX crystal with the largest at the site of the initial slot: just as with the previous sample. The one difference this time is that while most of these crack run horizontally left to right, some cracks begin to form vertically top to bottom. Finally, at t = 7.6 μs the cracks reach their full extent before the viewing window is cleared. At this point the crack at the slot location is prominent, however the largest crack appears vertically near the rear of the sample.

All of these slot samples aimed to examine the additional damage that may occur due to initial slots in the HMX crystals. The final three samples demonstrate that large cracks tend to extend from the initial defect sites. As discussed in the introduction, Duarte et al. showed that within this impact velocity regime (around 400 m/s) additional damage should occur at the defect sites and that this damage would lead to increased temperatures and hot spot formation [28]. While the temperatures cannot be measured, this additional damage is present. As for the angled lines formed in figure 3.13, further testing would be needed to determine the exact nature of the damage in the crystal. A future sample displaying the same behavior with a known impact plane would be helpful in this venture.

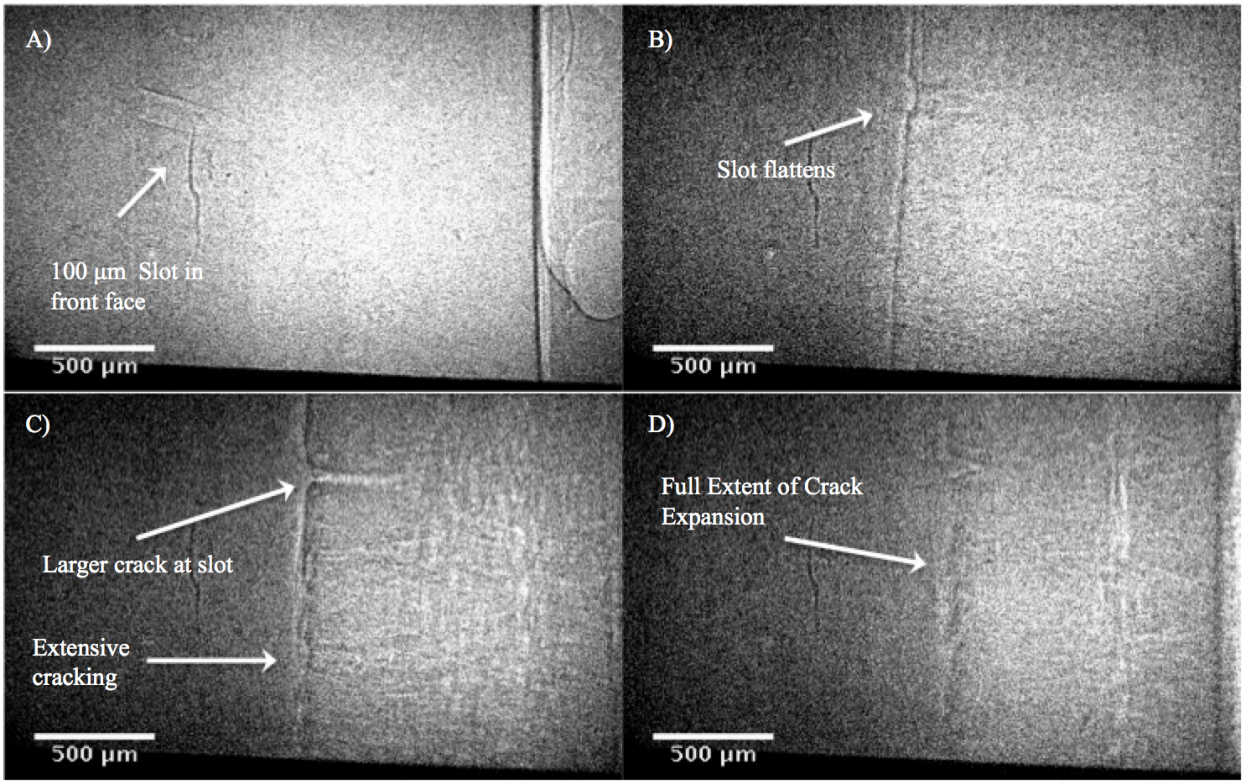

Figure 3.16. Image sequence of HMX containing a 100 µm milled slot impacted at 427 m/s at A) 0 µs, B) 4.2 µs, C) 6.6 µs, and D) 7.6 µs.

4. CONCLUSIONS

A single stage light gas gun was used to impact three different subsets of PBX samples at velocities ranging from 370 to 520 m/s using X-ray PCI to analyze the damage and deformation in real time. The impact conditions represent the maximum velocities available with the current gas gun setup and it was determined that higher velocities are likely needed to see consistent evidence of hot spot formation and growth. The first subset of samples contained multiple HMX particles in the Sylgard-184® matrix, both production grade and single crystals. The production grade samples showed significant damage as expected. Cracks and interfaces opened causing the particles to expand. Some of the open interfaces formed in a curved manor likely pointing to debonding between the HMX particles and the polymer matrix, however most appeared linear evidencing cracks. These samples acted similarly to the production grade single particles previously examined (particle expansion due to cracking and open interfaces) [10], but at lower impact velocities, likely due to increased stress concentrations from the particle-particle interactions occurring as the particles expanded into one another (i.e. damage seen in single particle experiments at 440 m/s was seen in multiple particle experiments at 400 m/s [10]). For the two crystal samples, evidence of cracking was observed originating from the crystal-crystal interface, most often spanning from the bottom left to the top right. In the final frame of figure 3.4, the top right corner of the rear crystal separated along these lighter lines, leading to the conclusion that these line were in fact cracks. Figure 3.6 showed an increased separation at the crystal-crystal interface, leading to what appears to be debonding (indicated by curves lighter lines). This separation was likely either caused by wave mechanics or a possible reaction.

The next subset of samples contained a drilled hole to simulate a void in the HMX. The first two samples discussed used large 500 μm holes to view how the holes collapsed. Figures 3.7 and 3.8 show that the holes primarily collapsed in a uniform manner (both down the length of the hole and at the circular end), however there was a slight rotation in the collapse from the end-on view of the hole. Overall, the as expected at this velocity, there was no evidence of a pore collapse mechanism that would lead to “jetting.” The next samples detailed two hole systems with 100 μm holes. These were set up to view the damage occurring behind the holes rather than the collapse of the holes themselves. A network of cracks formed behind each hole and expanded as they moved to the left. It was determined that this cracking behavior might be occurring in the

Sylgard-184® rather than the HMX crystal, but a bare crystal test eased these doubts (a vacuum chamber test should confirm this).

The final subset of samples contained a milled slot aimed to simulate an initial crack in the HMX. The first sample produced cracking at the slot location but also produced a series of crisscrossing angled lines throughout the sample before breaking apart. These lines did not appear as previous cracks have leading theory that the cracks may be held together (not opening) and that additional tests with known crystal orientation are needed. The other milled slot samples showed very similar behavior as distinct cracking occurred throughout the crystal, most prominently at the location of the milled slot. This increased damage where the initial defect occurred lines up with the modeling predictions that these initial cracks could lead to hot spot formation [28].

REFERENCES

[1] T. Zhou, J. Lou, Y. Zhang, H. Song, F. Huang, Hot spot formation and chemical reaction initiation in shocked HMX crystals with nanovoids: a large-scale reactive molecular dynamics study*, Physical Chemistry Chemical Physics***, 2016**.

[2] A. K. Sikder, N. Sikder, A review of advanced high performance, insensitive and thermally stable energetic materials emerging for military and space applications, *J. Hazard. Mater.* **2004**.

[3] V. J. Bellitto, M. I. Melnik, Surface defects and their role in the shock sensitivity of cyclotrimethylene-trinitramine*, Appl. Surf. Sci.***, 2010**.

[4] F. P. Bowden, A. Yoffe, Hot spots and the initiation of explosion*, Symposium on Combustion and Flame, and Explosion Phenomena***, 1948**.

[5] C. Coffey, R. Armstrong, Description of hot spots associated with localized shear zones in impact tests [Research Report, Oct. 1979 - Sep. 1980], **1981**.

[6] C. M. Tarver, S. K. Chidester, A. L. Nichols III, Critical conditions for impact- and shock-induced hot spots in solid explosives*, J. Phys. Chem.***, 1996**.

[7] J. E. Field, N. K. Bourne, S. J. P. Palmer, S. M. Walley, J. Sharma, B. C. Beard, Hot-Spot Ignition Mechanisms for Explosives and Propellants [and Discussion]*, Philosophical Transactions of the Royal Society: Physical and Engineering Sciences (1990-1995)***, 1992**.

[8] A. Barua, S. Kim, Y. Horie, M. Zhou, Ignition criterion for heterogeneous energetic materials based on hotspot size-temperature threshold*, J. Appl. Phys.***, 2013**.

[9] M. R. Baer, W. M. Trott, AIP Conference Proceedings, **2002**.

[10] N. E. Kerschen, C. J. Sorensen, Z. Guo, J. O. Mares, K. Fezzaa, T. Sun, S. F. Son, W. W. Chen, , X-Ray Phase Contrast Imaging of the Impact of a Single HMX Particle in a Polymeric Matrix*, Propellants, Explosives, Pyrotechnics***, 2019**.

[11] N. K. Bourne, A. M. Milne, The temperature of a shock-collapsed cavity*, Proceedings of the Royal Society A: Mathematical, Physical and Engineering Sciences***, 2003**.

[12] H. Czerski, W. G. Proud, Relationship between the morphology of granular cyclotrimethylene-trinitramine and its shock sensitivity*, J. Appl. Phys.***, 2007**.

[13] Van Der Heijden, H. B. Bouma, Crystallization and characterization of RDX, HMX, and CL-20*, Crystal Growth and Design***, 2004**.

[14] J. K. Dienes, Frictional hot-spots and propellant sensitivity*, Mater. Res. Soc. Symp. Proc.*, **1984**.

[15] D. Varfolomeev, K. Grebenkin, A. Zherebtsov, M. Taranik, Hot Surfaces in Heterogeneous Explosives Initiated by a Shock Wave*, Combust. Explos. Shock Waves*, **2010**.

[16] R. N. Mulford, J. A. Romero, AIP Conference Proceedings**, 1998**.

[17] S. M. Chitanvis, AIP Conference Proceedings, **2004**.

[18] E. M. Hunt, S. Malcolm, M. Jackson, , High-Speed Study of Drop-Weight Impact Ignition of PBX 9501 Using Infrared Thermography*, ISRN Mechanical Engineering*, **2011**.

[19] D. N. Preston, P. D. Peterson, L. Kien, Yin, D. E. Chavez, R. Deluca, G. Avilucea, S. Hagelberg, Effects of damage on non-shock initiation of HMX-based explosives, **2009**.

[20] C. Hua, P. Zhang, X. Lu, M. Huang, B. Dai, H. Fu, Research on the Size of Defects inside RDX/HMX Crystal and Shock Sensitivity*, Propellants, Explosives, Pyrotechnics*, **2013**.

[21] A. Kapahi, H. S. Udaykumar, Dynamics of void collapse in shocked energetic materials: physics of void-void interactions*, Shock Waves*, **2013**.

[22] M. A. Wood, D. E. Kittell, C. D. Yarrington, A. P. Thompson, Multiscale modeling of shock wave localization in porous energetic material*, Physical Review B*, **2018**.

[23] C. Duarte, A. Hamed, J. Drake, C. Sorensen, S. Son, C. W.W. Chen, M. Koslowski, Void Collapse in Shocked HMX Single Crystals: Simulations and Experiments*, Propellants, Explosives, Pyrotechnics*, **2020**.

[24] R. H. B. Bouma, A. G. Boluijt, H. J. Verbeek, van Der Heijden, On the impact testing of cyclotrimethylene trinitramine crystals with different internal qualities*, J. Appl. Phys.*, **2008**.

[25] F. P. Bowden, M. F. R. Mulcahy, R. G. Vines, A. Yoffe, The Detonation of Liquid Explosives by Gentle Impact. The Effect of Minute Gas Spaces*, Proceedings of the Royal Society of London.Series A, Mathematical and Physical Sciences (1934-1990)*, **1947**.

[26] J. K. Dienes, Q. H. Zuo, J. D. Kershner, Impact initiation of explosives and propellants via statistical crack mechanics*, J. Mech. Phys. Solids*, **2006**.

[27] B. Tanasoiu, M. Koslowski, A parametric study of the dynamic failure of energetic composites*, J. Appl. Phys.*, **2017**.

[28] C. A. Duarte, N. Grilli, M. Koslowski, Effect of initial damage variability on hot-spot nucleation in energetic materials*, J. Appl. Phys.*, **2018**.

[29] N. Grilli, C. A. Duarte, M. Koslowski, Dynamic fracture and hot-spot modeling in energetic composites*, J. Appl. Phys.*, **2018**.

[30] N. Grilli, M. Koslowski, The effect of crystal orientation on shock loading of single crystal energetic materials*, Computational Materials Science*, **2018**.

[31] N. Kedir, C. D. Kirk, Z. Guo, N. E. Kerschen, T. Sun, K. Fezzaa, W. Chen, Real-time visualization of impact damage in monolithic silicon carbide and fibrous silicon carbide ceramic composite*, Int. J. Impact Eng.*, **2019**.

[32] W. Chen, Z. Guo, M. Hudspeth, N. Parab, T. Sun, K. Fezzaa, High-speed X-ray PCI and XRD During Dynamic Fracture,*Procedia Engineering* **2017**.

[33] W. W. Chen, M. C. Hudspeth, B. Claus, N. D. Parab, J. T. Black, K. Fezzaa, S. N. Luo, In situ damage assessment using synchrotron X-rays in materials loaded by a Hopkinson bar*, Philosophical Transactions of the Royal Society A: Mathematical, Physical and Engineering Sciences*, **2014**.

[34] M. Hudspeth, B. Claus, S. Dubelman, J. Black, A. Mondal, N. Parab, C. Funnell, F. Hai, M. L. Qi, K. Fezzaa, S. N. Luo, W. Chen, , High speed synchrotron x-ray phase contrast imaging of dynamic material response to split Hopkinson bar loading*, Rev. Sci. Instrum.*, **2013**.

[35] M. Hudspeth, T. Sun, N. Parab, Z. Guo, K. Fezzaa, S. Luo, W. Chen, Simultaneous X-ray diffraction and phase-contrast imaging for investigating material deformation mechanisms during high-rate loading*, Journal of Synchrotron Radiation*, **2015**.

[36] N. E. Kerschen, *Investigation into High Explosive Particle Dynamics under Impact Loading*, Ann Arbor : ProQuest Dissertations & Theses **2018**.

[37] N. D. Parab, Z. A. Roberts, M. H. Harr, J. O. Mares, A. D. Casey, I. E. Gunduz, M. Hudspeth, B. Claus, T. Sun, K. Fezzaa, S. F. Son, W. W. Chen, High Speed X-ray Phase Contrast Imaging of Energetic Composites under Dynamic Compression*, Purdue Energetics Research Center Articles*, **2016**.

[38] N. D. Parab, B. Claus, M. C. Hudspeth, J. T. Black, A. Mondal, J. Sun, K. Fezzaa, X. Xiao, S. N. Luo, W. Chen, Experimental assessment of fracture of individual sand particles at different loading rates*, Int. J. Impact Eng.*, **2014**.

[39] S. J. Turneaure, Y. M. Gupta, Real time synchrotron x-ray diffraction measurements to determine material strength of shocked single crystals following compression and release*, J. Appl. Phys.*, **2009**.

[40] B. J. Jensen, S. N. Luo, D. E. Hooks, K. Fezzaa, K. J. Ramos, J. D. Yeager, K. Kwiatkowski, T. Shimada, D. M. Dattelbaum, Ultrafast, high resolution, phase contrast imaging of impact response with synchrotron radiation*, AIP Advances*, **2012**.

[41] S. N. Luo, B. J. Jensen, D. E. Hooks, K. Fezzaa, K. J. Ramos, J. D. Yeager, K. Kwiatkowski, T. Shimada, Gas gun shock experiments with single-pulse x-ray phase contrast imaging and diffraction at the Advanced Photon Source*, Rev. Sci. Instrum.*, **2012**.

[42] N. D. Parab, Z. Guo, M. Hudspeth, B. Claus, B. H. Lim, T. Sun, X. Xiao, K. Fezzaa, W. W. Chen, In situ observation of fracture processes in high-strength concretes and limestone using high-speed X-ray phase-contrast imaging*, Philosophical Transactions of the Royal Society.A, Mathematical, Physical and Engineering Sciences*, **2017**.

[43] N. D. Parab, J. T. Black, B. Claus, M. Hudspeth, J. Sun, K. Fezzaa, W. W. Chen, Observation of Crack Propagation in Glass Using X-ray Phase Contrast Imaging*, International Journal of Applied Glass Science*, **2014**.

[44] X. Zhai, J. Gao, Y. Nie, Z. Guo, N. Kedir, B. Claus, T. Sun, K. Fezzaa, X. Xiao, W. W. Chen, Real-time visualization of dynamic fractures in porcine bones and the loading-rate effect on their fracture toughness*, J. Mech. Phys. Solids*, **2019**.

[45] W. W. Chen, M. C. Hudspeth, B. Claus, N. D. Parab, J. T. Black, K. Fezzaa, S. N. Luo, In situ damage assessment using synchrotron X-rays in materials loaded by a Hopkinson bar*, Philosophical Transactions of the Royal Society A: Mathematical, Physical and Engineering Sciences*, **2014**.

[46] Mason & Hanger-Silas, Mason Co, Pantex Plant, (U. S.), United States Dept of Energy Office of Scientific and, Technical Information, *Background material properties of selected silicone potting compounds and raw materials for their substitutes*, Pantex Plant (U.S.); distributed by the Office of Scientific and Technical Information, U.S. Dept. of Energy, Amarillo, Tex. : Oak Ridge, Tenn., **1978**.

[47] I. D. Johnston, D. K. McCluskey, C. K. L. Tan, M. C. Tracey, Mechanical characterization of bulk sylgard 184 for microfluidics and microengineering*, Mechanical characterization of bulk Sylgard 184 for microfluidics and microengineering*, **2014**.

[48] M. Cawkwell, T. Sewell, L. Zheng, D. L. Thompson, Shock-induced shear bands in an energetic molecular crystal: Application of shock-front absorbing boundary conditions to molecular dynamics simulations*, Physical Review B*, **2008**.

[49] C. Blum-Sorensen, HMX Unit Cell, **2020**.

[50] M. Nikl, Scintillation detectors for x-rays, *Review Article,* **2006**.

PUBLICATIONS

[1] C. Duarte, A. Hamed, J. Drake, C. Sorensen, S. Son, W. Chen, M. Koslowski, Void Collapse in Shocked HMX Single Crystals: Simulations and Experiments, *Propellants, Explosives, Pyrotechnics*, **2020**.

[2] N. Kerschen, J. Drake, C. Sorensen, Z. Guo, J. Mares, K. Fezzaa, T. Sun, S. Son, W. Chen. *X-ray Phase Contrast Imaging of the Impact of Multiple HMX Particles in a Polymeric Matrix.* Manuscript accepted for publication in Propellants, Explosives, and Pyrotechnics, **2020**.